IISc Theses Abstracts

Contents

J. Indian Inst. Sci., Nov.–Dec. 1994, **74**, 781–840.

IISc THESES ABSTRACTS

Thesis Abstract (Ph.D.)

A study of circumstellar silicon monoxide masers by Nimesh A. Patel

Research supervisors: Arnab Rai Choudhuri and V. Radhakrishnan (RRI)
Department: Physics

1. Introduction

This work presents an observational study of about 170 Mira variables, which are pulsating red giants. Observations were carried out at the frequency of 86.2 GHz which corresponds to $v = 1$, $J = 2$–1 transition in SiO. The aim was to study the dependence of the maser phenomenon on the intrinsic properties of the Mira variables like spectral type, luminosity, evolutionary stage, amplitude of pulsation and infrared spectrum. A historical introduction to the subject of observations of molecules at millimeter wavelengths is included and the properties of Mira variables and some characteristics of the SiO maser emission are reviewed.

2. Pointing and gain calibration of the RRI 10.4-m telescope

Since the observations reported in this work are the first ones made using the Raman Research Institute's 10.4-m millimeter-wave telescope, its instrumental characteristics and pointing and gain calibration, some aspects of which are peculiar to this telescope, are presented in detail.

3. Calibration errors

The performance of the telescope is evaluated by observing some standard sources, and the errors in the measurement of absolute fluxes are estimated.

4. Observations

The method of observations is described. Tables of results and spectral lines are given. The sources were mainly selected from the General Catalogue of Variable Stars[1] and from the NASA IR catalogue[2]. Among the seven new detections, a surprising result is that of T Cnc, which is a unique carbon star, in showing the SiO maser emission. T Cnc belongs to the group of carbon stars which are unusual in showing the presence of an oxygen-rich atmosphere[3], as indicated from their infrared spectra.

5. SiO maser luminosity and its dependence on the intrinsic properties of the Mira variables

To know the relation between the maser phenomenon and any intrinsic property of the Mira variable, one must convert the observed maser flux from a source into luminosity, for which one needs to know the distance to the source. The known methods for determining distances to the Mira variables are reviewed. Distances are calculated from a comparison of the apparent infrared magnitude at 2.2 microns[2], and the absolute magnitude obtained from a period-luminosity relation[4]. The observed fluxes are then converted to luminosities, after correcting for all telescope losses.

6. Conclusions and interpretations

The results of this study can be summarized as follows:

1. Not all Mira variables show the SiO maser emission. The masing M-giant Mira variables are restricted in the range of mean spectral types M6–M10.

2. The maser luminosity is also found to be correlated with the bolometric magnitude.

3. In the H–R diagram, it is found that the masing Mira variables are restricted in a region described by the limits: $M_{bol} \leq -4.8$ and $\log T_{eff} \leq 3.48$. This can be interpreted as implying a lower limit of $\sim 300 R_{\odot}$ to the radius of a masing star.

4. There is an indication of an anti-correlation between the SiO photon-luminosity and the amplitude of pulsation in the visual magnitude.

We discuss these results and suggest some interpretations. The cut-off in the maser luminosity below M6 may be due to a lack of SiO abundance in these stars. The decrease in maser luminosity for stars having large pulsational amplitudes may be due to a shorter coherence length as suggested by a correlation between the expansion velocity of circumstellar matter with the amplitude of pulsation. The correlation of maser luminosity with bolometric magnitude suggests a radiative pump mechanism. We show that the radiative pump mechanism is consistent with several other observations, as well as with the theoretical model atmosphere of a typical Mira variable[5]. Some strong masers for which the radiative pump had failed to produce the observed maser-power; we suggest an additional source of pump photons to be the circumstellar dust shell. This is suggested by the observation of optically thick dust shells around these stars[6].

References

1. KHOLOPOV, P. N., *et al* — *General catalogue to variable stars*, 1985, Moscow Publishing House.
2. GEZARI D. Y., *et al.* — *Catalogue of infrared observations*, 1987, NASA Reference Publication 1196.
3. LLOYD-EVANS, T. — *Mon Not. R. Astr. Soc.*, 1990, **243**, 336–348.
4. FEAST, M. W. — *Mon. Not. R. Astr. Soc.*, 1984, **211**, 51p–55p.
5. BOWEN, G. H. — *Astrophys. J.*, 1988, **329**, 299–317.
6. ROWAN-ROBINSON, M. AND HARRIS, S. — *Mon. Not. R. Astr. Soc.*, 1983, **202**, 767–795.

Thesis Abstract (Ph.D.)

Studies on hetero-redundant architecture for the input processing sub-system and the boundary controller of a digital flight control computer by C. Subramanian

Research supervisors: D. K. Subramanian and Kota Harinarayana (HAL/ADA)
Department: Computer Science and Automation

1. Introduction

Designers of modern aircraft have been developing new approaches for digital flight control systems (DFCSs) in order to meet the specified performance and reliability requirements. New control functions to achieve short runway performance through thrust-vectoring, fuel efficiency, etc., are being continuously evolved at a rate which subdues the potential for reliability improvements of these systems. Various approaches to improve the reliability of the components of DFCS are being contemplated. The flight control computer (FCC) being a vital component of DFCS, its design demands incorporation of sound fault-tolerant approaches to achieve the required level of reliability. Due to the reliability characteristics of its electronic hardware and software, most of the current FCC architectures incorporate multiple redundancy. However, they do not have handlers to solve problems due to near-coincident errors, instantaneous failures, absence of integrity check mechanisms, etc. There have been attempts to reduce the risks due to coincident errors by running of channels in loose synchronism[1] and incorporation of dissimilar software[2]. The experimental results on dissimilar software also show that the assumption of independence of versions is quentionable[3] and hence, its reliability too. Hence, the search continues for new fault-tolerant approaches.

2. Thesis contribution

The main contribution is in the area of architecture, its performance evaluation and reliability estimation as discussed below.

2.1. *Architecture*

The basic aim of the research was to evolve an FCC architecture incorporating the functional components of IPS-PAC (input processing sub-system for pitch axis control), BC (boundary controller), voter and INVC (INVerse calculator), which would overcome some of the problems cited earlier. The design of this architecture introduces heterogenity in its components of hardware and software from the conceptual stage onwards to derive advantages of reliability and fault tolerance. Hence, it is known as hetero-redundant architecture (HHH). The FCC architecture (Fig.1) employs (I) four heterogeneous approaches for input data processing (IDP), *viz.*, MEU (modified Euler), RK4 (Runge Kutta-4), KF (Kalman filter) and CONV (CONVentional), (ii) boundary controllers (BCs) which could be based on either bit-map of maximal blocks approach, (iii) RM (redundancy management) and WA (weighted average) voting and INVC for its integrity check, and (iv) INTP (interpolator) which interpolates stored data for IDP.

Based on the current practices in VLSI, realization schemes[4] for each of the functional components of IDP, BC and INVC are also drawn and their computational sizings are estimated.

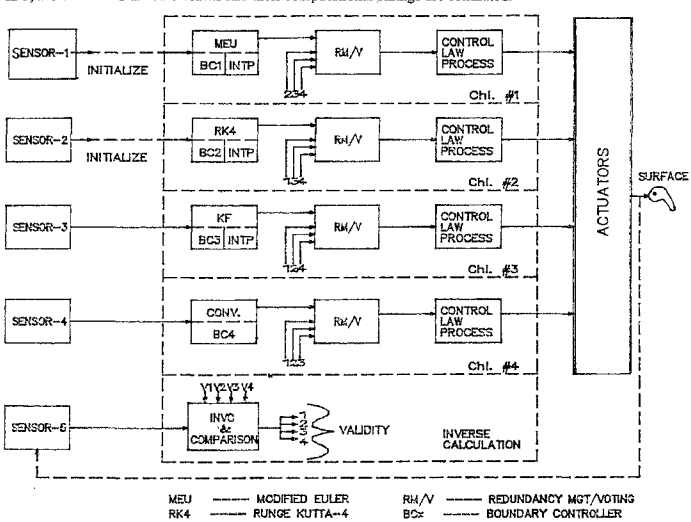

FIG. 1. Schematic of hetero-redundant architecture of flight control system.

2.2. *Performance evaluation*

The evaluation of performance of approaches of IDP, BC and INVC was conducted through digital flight stimulation exercises with respect to longitudinal axis of aircraft, angle of attack (α) and pitch rate (q) being

taken as the aircraft states. Monte Carlo simulation was resorted to evaluate the performance of RM and voting schemes.

The IDP approaches, *viz.*, MEU, RK4 and KF, were found to satisfy the performance measures of response-time and error-boundedness. The response generated by the methods MEU, RK4 and KF closely follow each other and the maximum difference between values of aircraft states generated by them is 1%. KF being superior to others due to its filtering characteristics, is taken as the reference for comparisons. It has been found to reduce the noise and smoothen the states under all flight conditions. In the case of instantaneous failures, the ratio of the error with KF to that with RK4 approach is of the order of 0.4. This is due to the Markovian property of the filter[5].

The analysis of results of simulation exercises on two types of voting schemes[6], *viz.*, median select and weighted average and RM shows that:

i) For both the voting schemes the noise in the voted output is less than the noise in any of the channels except the channel with no noise. This is because the voting rejects the channel with high noise.

ii) In general, the output noise generated by WA scheme is less than that generated by the median select scheme.

iii) WA scheme provides continuous output and smoothens failure-transition and isolation, whereas, median select introduces undesirable transients due to channel switching.

The response of the aircraft under the operations of the boundary controllers based on bit-map as well as maximal blocks approaches was within acceptable tolerance limits[7]. The identification of boundary exceedences under these approaches is based on the flight parameters M (Mach no,), H (altitude) and N_Z (Normal acceleration), which are sensed more accurately than α. These new approaches prevented the tendency for boundary exceedences and also facilitated safe operation nearer to the boundaries of flight envelope. Pilot intervention would also be totally eliminated.

2.3. *Reliability estimation*

Reliability analysis and estimation have been carried out on the proposed architecture through techniques based on combinatorics, Markov process and Petri-net. Combinatorial technique and Markov process were used to obtain transient state reliability measures, whereas Petri-net model was used to get steady-state reliability measures.

The transient reliability of the conventional system is higher than that of conventional system. The difference between them is high when both of them are perfect compared to when one failure has occurred in either of them. In the two-failures case, the difference between the reliabilities is marginal, *i.e.*, in the worst case both the reliabilities are more or less equal.

Under steady-state reliability estimation, the minimum sojourn time of a tangible state in the proposed system is found to be 1.66 times of that in a conventional system. The time taken to reach an absorbing state from a transient state in the proposed system is more than that in the conventional system. A transient state is visited more number of times in the proposed system compared to the conventional system. Together both these findings imply that the proposed system would function longer in a transient state compared to the conventional system.

3. Conclusions

As the real-time response and errors under steady state and transient conditions are within acceptable limits, the approaches of MEU, RK4 and KF are acceptable.

Under the flight conditions studied both the BC approaches were more efficient and effective than the existing ones. However, due to its simplicity and elegance bit-map would be preferable.

The WA voting is preferred due to its better performance compared to median-select. Its performance would still improve with effective monitoring, rejection and reacceptance strategies. The INVC module facilitates to ensure integrity of voter which is the hardcore of FCC.

The cyclomatic complexity measures of software modules of IPS_PAC, BC and INTP are found to be below 10, and hence their levels of reliability would be high.

Both the performance and reliability of the proposed architecture have been found to be better than the conventional one.

For further research, several new directions such as performance evaluation of IPS-PAC, BC, etc., based on flight test results, and further studies on INVC, etc. are indicated.

References

1. WENSLEY, J. H., *et al.* SIFT: Design and analysis of a fault-tolerant computer for aircraft control, *Proc.IEEE.*, 1978, **66**, 1240–1255.

2. AVIZIENIS, A., *et al.* On the implementation of N-version programming for software fault tolerance during execution, *Proc. COMPSAC, 77*, pp. 149–155.

3. KNIGHT, J. C., *et al.* An experimental evaluation of the assumption of independence in multi-version programming, *IEEE Trans.*, 1986, **SE–12**, 96–109.

4. YEH, H. G. Systolic implementation of Kalman filter, *IEEE Trans.*, 1988, **ASSP–1**, 1514–1517.

5. SUBRAMANIAN, C. AND SUBRAMANIAN, D. K. Hetero-redundant architecture with Kalman filter for input-processing in flight control system, 18th *ICAS Congr*, Beijing, Sept. 20–25, 1992.

6. SUBRAMANIAN, C. AND SUBRAMANIAN, D. K. Performance analysis of voting strategies for a fly-by-wire systems of a flighter aircraft, *IEEE Trans.*, 1989, **AC-34**, 1019–1021.

7. SUBRAMANIAN, C. AND SUBRAMANIAN, D. K. Evaluation of boundary controllers based on bit-map and quad-tree for a fighter aircraft, *AMSE: Modeling, Simulation & Control, C*, 1991, **24**, 9–22.

Thesis Abstract (Ph.D.)

Optimal synthesis of shell and tube heat exchangers by K. Ramananda Rao

Research supervisors: U. Shrinivasa and J. Srinivasan
Department: Mechanical Engineering

1. Introduction

Optimal synthesis of engineering systems has become important in recent years due to the ever-increasing costs of materials, labour and energy. However, many mechanical systems have large numbers of parameters to be determined and large numbers of constraints to be satisfied. The interrelationships between the parameters and the chosen objective functions are usually complicated and very rarely expressible in algebraic forms. Under these circumstances, there is a need for the development of special-purpose algorithms to handle each specific class of problems. In this work, we investigate the possibility of developing such algorithms for the optimal synthesis of shell and tube heat exchangers. The objective functions considered are capital cost, total cost, weight and volume along with heat duty, geometric constraints, pressure drop limitations and velocity restrictions as constraints.

Over the years, a large number of methods have been proposed to optimize different types of heat exchangers. Many authors have used Lagrange multiplier and geometric programming methods which require explicit expressions for the objective function and the constraints. Different search methods have been employed and Palen *et al.*[1] have proposed a case study method for optimization. These methods are more effec-

tive when approximate global minimum is known a priori. Johnson *et al.*[2] have used nonlinear optimization codes like COPES/CONMIN to optimize single-pass shell and tube condensers. Though these methods can handle objective functions and constraints even in the form of procedures, they do not ensure convergence to the global optimum and at times even fail to provide a feasible design[3].

The shell and tube heat exchanger optimization problem can be formulated as follows. Minimize objective function F subject to

specified heat duty $g_1 \geq QR$,

geometric constraints $g_{2i} \geq 0$, $1 \leq i \leq N_g$,

Pressure drop limitations $g_{3j} \leq GP_j$, $j = 1$ or 2

(1 = tube side and 2 = shell side),

velocity restrictions $g_{4k} \leq GV_k$, $k = 1$ or 2

(1 = tube side and 2 = shell side),

where

$F = F(DS, DT, LTP, LBC, LTO, NTP, THETATP)$,

$g_1 = g_1$ (fluid specifications, DS, DT, LTP, LBC, LTO, NTP, $THETATP$),

$g_{2i} = g_{2i}$ (DS, DT, LTP, LBC, LTO, NTP, $THETATP$),

$g_{3j} = g_{3j}$ (fluid specifications, DS, DT, LTP, LBC, LTO, NTP, $THETATP$),

$g_{4k} = g_{4k}$ (mass flow rates of fluids, DS, DT, LTP, LBC, LTO, NTP, $THETATP$),

QR = head duty demanded by the process specifications,

N_g = number of geometric constraints,

Gp_j = allowable pressure drops,

Gv_k = velocity restrictions,

DS = shell diameter,

DT = outside tube diameter,

LTP = tube layout pitch,

LBC = baffle spacing,

LTO = overall exchanger length,

NTP = number of tube passes,

$THETATP$ = tube layout characteristic angle.

For a particular problem, the fluids and their mass flow rates are known a priori. The optimization involves the selection of suitable values of the major geometric parameters, DS, DT, LTP, LBC, LTO, NTP and $THETATP$, such that the objective function is minimized.

2. Study of feasible designs

An exhaustive study of the structure of a large number of feasible designs of shell and tube heat exchangers generated for different process specifications revealed the existence of a unique feature in the near-optimal region. There the objective function was observed to be weakly coupled to the overall heat-transfer coefficient Uo as shown in Fig. 1 for the feasible designs generated for a typical set of specifications from an industry. The figure shows the existence of many designs in the near-optimal region with large variation in the values of Uo. Since the objective function is strongly dependent on geometry, the above phenomenon suggests that we could decouple the geometry and heat-transfer aspects during optimization.

We have carried out analytical investigations to ascertain our hypothesis of decoupling which gives us the following conditions for decoupling.

$$\frac{\partial \ln(Uo)}{\partial(\text{geometric parameter})} \simeq 0, \tag{1}$$

or

$$\frac{\partial \ln(Uo)}{\partial(\text{geometric parameter})} << \frac{\partial \ln(Ao)}{\partial(\text{geometric parameter})}, \tag{2}$$

where

C = the objective function

Ao = the exchanger surface area, m^2

Uo = the overall heat transfer coefficient, W/m^2 K

Parameter = any of the major exchanger geometric parameters such as shell diameter, tube diameter, pitch and baffle spacing.

It was observed that the condition represented by eqn 1 holds good for different cases (where the heat transfer is controlled by the thermal resistances due to shell side, tube side, fouling and controlled equally by the shell and tube side resistances) thus substantiating the existence of the decoupling phenomenon is heat exchanger optimization.

3. Basic algorithm

The decoupling simplifies the problem dramatically. At first, we need to consider only geometry optimization satisfying only the geometric constraints. This problem is comparatively simple and we were able to obtain even approximate analytical solution.

This geometry optimization module was properly linked to the thermal rating module to obtain optimal designs satisfying a given heat duty. A basic algorithm for this task has been developed and is explained by the flowchart given in Fig. 2. The basic algorithm works as follows. First an estimate of Uo is made from the given process specifications. From this, the required surface area Ao is calculated. A geometry is synthesized for this Ao minimizing the objective function by the geometry optimization module. For this geometry again Uo is evaluated. This process is repeated till convergence is achieved.

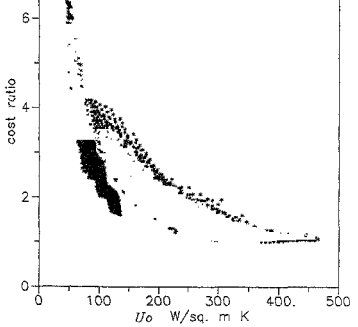

FIG. 1. Variation of objective function with Uo.

The near-optimal design obtained as above may not satisfy the velocity and pressure drop restrictions. Therefore, guidelines have been provided to modify this near-optimal deisgn to satisfy these constraints based on which several sub-algorithms were developed.

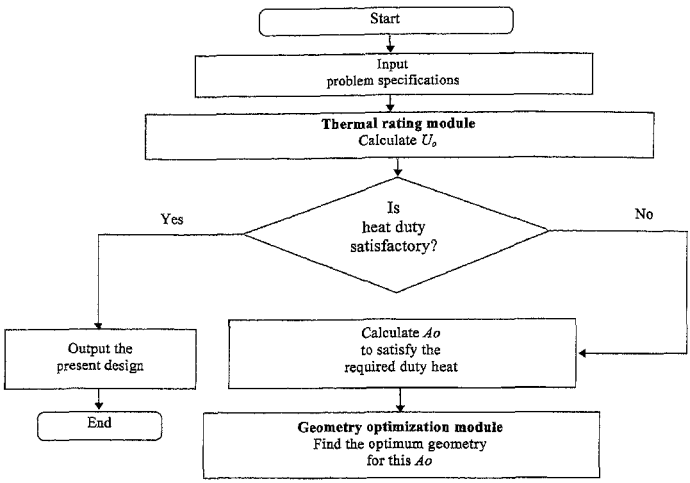

FIG. 2. The basic algorithm.

4. Conclusions

The final outcome of the present work is a basic algorithm and a host of sub-algorithms coupled to it for the optimal synthesis of shell and tube heat exchangers. The former delivers a near-optimal design which will be modified when necessary by the sub-algorithms to provide a design which satisfies velocity and pressure drop restrictions. The algorithms are quite simple and can easily be adapted to even manual calculations. The methodology is quite general and can handle various objective functions such as cost, weight and volume.

References

1. PALEN, J. W., CHAM, T. P. AND TABOREK, J. — *AICHE Symp. Ser*, 1974, **70**, 205–214.

2. JOHNSON, C. M., VANDERPLAATS, G. N. AND MARTO, P. J. — *Trans. ASME–J. Mech. Des.*, 1980, **102**, 469–475.

3. HANSEN, P., JAUMARD, B. AND LU, S. H. — *Trans. ASME–J. Mech., Transmissions, Autom. Des.*, 1989, **111**, 361–367.

Thesis Abstract (Ph. D.)

Multidimensional modelling of uniflow scavenging in two-stroke engines by M. R. Ravi

Research supervisor: A. G. Marathe
Department: Mechanical Engineering

1. Introduction

Two-stroke engines are superior to four-stroke engines in respect of the power output-to-engine weight considerations, and hence are widely used in two-wheeler automobiles. The main drawback with these engines is that since the intake of fresh charge and exhaust of burnt gases are simultaneous, a certain quantity of fresh gases escape through the exhaust, or, a certain quantity of burnt gases remain in the cylinder at the end of the gas exchange. The former is called short-circuiting and it results in the dilution of combustible charge in the cylinder, leading to inferior and incomplete combustion and reduced power output.

This drawback has to be minimized by suitably designing the cylinder geometry such that short-circuiting is minimized and residual gas pockets are not detained. For an effective scavenging process, the fresh charge must sweep through the entire volume of the cylinder, and very little fresh charge should escape through the exhaust. This needs a careful design of the cylinder geometry. A computer simulation program capable of predicting scavenging, given the geometry, would be a handy tool for such a design. The present work involves the development of such a prediction tool from basic laws of fluid mechanics and conservation of energy.

2. Literature review

Not many researchers have worked on multidimensional modelling of scavenging process. Carapanayotis and Salcudean[1,2] model scavenging process in the absence of piston motion. Sweeney *et al.*[3] use the PHOENICS computer program to model scavenging in five engine geometries to evaluate them critically. Diwakar[4,5] and Uzkan[6,9] have studied uniflow scavenging in the EMD 710 turbocharged diesel engine of the General Motors, to study the effects of engine swirl, speed and stroke on the scavenging characteristics.

In the analysis of scavenging, the initial pressure and temperature values inside the cylinder are critically important, since these values determine the mass of fresh charge delivered to the cylinder, and thus the scavenge ratio. In diesel engines, pure air is aspirated and diesel is sprayed into the cylinder, while in carbureted engines, a mixture of fuel and air is aspirated. The analysis methodology for the two kinds of engines needs to be different.

No literature is available on the multidimensional simulation of scavenging in carbureted engines. Diwakar[4,5] and Uzkan[6,9] present the analysis of a diesel engine, assuming the same initial thermodynamic state for various values of parameters analyzed.

The present work analyzes a carbureted engine with the same dimensions to illustrate why the analysis needs to be different from that for a diesel engine. A parametric study on the effect of various geometric and operating parameters of the engine on its gas exchange characteristics has also been conducted.

3. Problem formulation

A geometry as shown in fig. 1 is chosen for the analysis of the present work. The cylinder has an inlet port in the form of a sleeve on the side walls, and an exhaust port opening in the form of an annular slot on the cylinder head. On this axisymmetric geometry, the problem is solved by splitting it into two parts: (i) the global part, which computes the gross mass flow rates across the inlet and exhaust ports compressible orifice flow equations and the cylinder pressure and temperature using global mass

and energy conservation, and (ii) the local part, which uses the results of the global part as boundary conditions to solve axisymmetric Navier–Strokes equations, energy equation and species conservation equations and obtain the flow field information. Turbulence is modelled using a zero-equation eddy viscosity model. Combustion is represented as a stoichiometric heat release phenomenon[10].

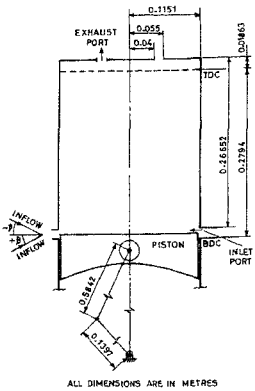

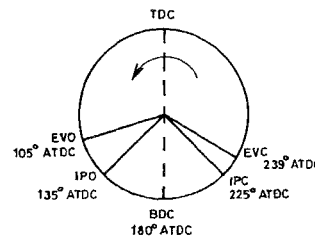

Fig. 1. Geometry and timing diagram.

A computer program called CARE (cyclic analysis of reciprocating engines) has been developed to implement the above analysis procedure. The code has been validated by comparing the results of a test case with that of Diwakar[5].

4. Results

In carbureted engines, the amount of fuel inducted into the cylinder is directly proportional to the delivery ratio, and hence, the heat release is determined by the mass of charge aspirated. This is in contrast to the diesel engines where pure air is inducted and fuel is sprayed in after compression. Hence, the scavenging and heat release are intimately coupled in carbureted engines, and the equations governing them need to be solved simultaneously. This is proposed to be accomplished by running the simulation over many cycles until the global quantities repeat themselves periodically over the cycles. Ravi *et al.*[11] describe in detail the importance of this cyclicity of the solutions to the prediction of gas exchange phenomenon.

A parametric study on the effect of the inlet port size, exhaust port size, inlet swirl, inlet inclination with piston plane, engine speed, inlet manifold pressure, exhaust manifold pressure and timing of exhaust valve closure on the flow field and global quantities has been carried out. It is found that since an increase in inlet area results in an increase in the duration for which the inlet port is open, delivery improves and trapping deteriorates. Increase in exhaust area results in lower resistance to inflow, leading to an improvement of delivery and scavenging and deterioration of trapping[12]. An increase in inlet pressure and decrease in exhaust pressure have the same effects on scavenging parameters. Engine speed also determines the time-area for inflow and outflow, and so a decrease in engine speed leads to the same above effects.

Increase in inlet swirl results in the fresh charge crowding at the cylinder walls, leaving a core of burnt gases at the axis. A positive inclination angle (upward inflow) has the same effect, but a

negative inclination results in better replenishment of charge in the central region. Scavenging, delivery and trapping are not affected to a significant extent by these two parameters. Timing of exhaust closure affects only the terminal phase of scavenging, and dictates the extent of short-circuiting and hence trapping.

5. Conclusions

A novel method is proposed and implemented on a new computer program CARE for cyclic analysis of reciprocating engines. Importance of running the simulation to cyclicity is established, and a parametric study has been carried out. It is found that parameters which result in an improvement of delivery or decrease in resistance to inflow influence scavenging to a large extent than those which affect only the charge distribution in the flow field.

References

1. CARAPANAYOTIS, A. AND SALCUDEAN, M. — *ASME-FED*, 1988, **5**, 75.
2. CARAPANAYOTIS, A. AND SALCUDEAN, M. — *J. Engng Gas Turbines Power*, 1988, **110**, 538–546.
3. SWEENEY, M. E. G., SWANN G. B. G., KENNY R. G. AND BLAIR, G. P. — *SAE* 850519, 1985.
4. DIWAKAR, R. — *ASME-FED* 28, 1985.
5. DIWAKAR, R. — *SAE* 870596, 1987.
6. UZKAN, T. AND HAZELTON, J. R. — *SAE* 860466, 1986.
7. UZKAN, T. — *J. Engng Gas Turbines Power*, 1987, **109**, 459–464.
8. UZKAN, T. — *ASME-FED* 65, p. 67, 1988.
9. UZKAN, T. — *J. Engng Gas Turbines Power*, 1988, **110**, 523–530.
10. RAVI, M. R. AND MARATHE, A. G. — In *Computational modelling of free and moving boundary problems*, Vol. 2, (Wrobel, L. C and Brebbia, C. A., eds) Computational Mechanics Publications, 1991.
11. RAVI, M. R. AND MARATHE, A. G. — *ASME Energy sources Technol. Cong. and Exposition*, January 1992.
12. RAVI, M. R. AND MARATHE, A. G. — *SAE Int. Cong. and Exposition*, February 1992.

Thesis Abstract (Ph.D.)

Self-routing in some novel photonic switching architecture by Subrat Kar

Research supervisor: A. Selvarajan
Department: Electrical Communication Engineering

1. Introduction

The current motivation for research on photonic switching stems from two basic factors—for one, the need for ultrafast switching technology and secondly, for a common technology for the transmission and switching of photonic data streams. The significant inroads made by the optical fiber into higher capacity data highways provide further incentive for the switching of data streams in the optical incentive for the switching of data

streams in the optical domain and the development of photonic switching architectures(PSAs)[1]. Moreover, at the ultrafast data rates which shall be routinely demanded in the near future, it is only in the optical domain that the requisite data rate transparency can be achieved. While all-optical implementation remains the technology of the future, a first step for the present is a straight replacement of electronic switches by optical ones, such that the electrical overlay network processes the stripped headers and sets the homologous optical switch. In this approach, an electrical to optical conversion, and the associated bottleneck imposed by the driving electronic circuitry is inevitable. Optical self-routing of data, in some sense, bypasses the electrical overlay network and utilizes more effectively the bandwidth made available by the optical switching fabric.

2. Main contributions

This work addresses the issues involved in the design, layout and self-routing characteristics of some novel photonic switching architecture. The various issues addressed include the comparison of architectures known in the electronic domain and their suitability for implementation using integrated optic photonic switching element, the fault tolerance aspects of various switching architectures, some novel architectures and their properties and various issues relating to self-routing in photonic switching.

One of the main contributions of the work is the design and analysis of a family of new architectures called the SSpiral. The SSpiral are a class of annular architectures which are robustly fault tolerant, utilise substrate real estate efficiently and can emulate other architectures[2]. Closed-form expressions for the signal-to-crosstalk ratio and differential insertion loss are derived and the maximum size of the architectures realizable inferred from these Some members of this family allow binary self-routing in which the destination tag precedes the data and consists of a string of binary digits, one for each switch the signal passes through. In addition, one such member of this family, the CNet, was found to allow larger scales of integration than previously reported. The applicability of the members of this family as topologies for parallel processing configurations is also highlighted. The reliability of the CNet is estimated and the fault tolerance is measured in terms of a newly defined figure of merit called the normalized fault tolerance.

For purposes of the generation of photonic switching architectures and to achieve optimal layout, two special design programs PAD (photonic architecture designer) and PAL (photonic architecture layout) were developed. The simulated annealing algorithm is used as a basis for the placement and a study of the several constraints unique to photonic switching architectures is done. It was found that the problem of placement on optical substrates is not exactly identical to that of the placement of custom macro cells in the electronic domain. Some new architectures generated by the PAD program developed in this study are presented.

Self-routing in photonic switching is an area of current interest, and several techniques developed by the author for self-routing in PSAs are outlined. These include binary self-routing in the CNet, a two-wavelength scheme in which the header and the data are coded on two distinct fixed wavelengths, use of an integrated optic device called pulse-interval-coded optical content-addressable memory (PICOCAM) and others. It is shown that the PICOCAM structure can either be fabricated using tapped optical fibers or an integrated optic approach. Several alternative integrated optic implementations of the PICOCAM structure were considered: use of asymmetric taps (with the tap angle decided from Beam Propagation Method of simulation); use of half-directional couplers (3 dB couplers); and use of an array of PICOCAM structures with integrated optic directional couplers and optical orthogonal codes (OOCs). A scheme of all-optical implementation of a self-routing node is also studied using interference filters as the basic switching elements. The advantages and limitations of each proposed scheme are highlighted.

3. System aspects

The system aspects of using the various PSAs theoretically investigated in this work need also an understanding of the various experimental techniques. With this in view an attempt was made to fabricate the PICOCAM. The calculated mask coordinates and the method of fabrication are given. Liquid crystal RT (reflective/transmissive) elements were also investigated for use as optical interconnects. The use of a 4×4 CNet as a video distribution switching unit is suggested since such a scheme will result in high throughput.

4. Conclusions

In this work, focus was on some novel photonic switching architectures and the methods of self-routing in such switch fabrics. Design software packages were specifically developed for generating the switch fabrics.

Though all the examples considered in this work are based on $LiNb0_3$ material, it may be emphasized that devices based on GaAs and InP are fast emerging as viable alternatives. Hence, these materials also need further study.

References

1. SUBRAT KAR AND SELVARAJAN, A. — Some novel photonic guided wave space switching architectures, *Instn. Electron. Telecommun. Engrs.*, 1990, **36**, 513–519.

2. SUBRAT KAR AND SELVARAJAN, A. — Generation of Ti:$LiNbO_3$ directional coupler based photonic switching architectures with optimal substrate area utilisation, *Proc. SPIE, OE/FIBERS '89*, (Vol. 1177), *Int. Conf. on Integrated Optics and Optoelectronics*, Boston, MA, Sept. 5–8, 1989, pp. 111–122.

Thesis Abstract (M.Sc. (Engng))

Studies on interpenetrating polymer networks as binders for solid propellants by S. Parthiban

Research supervisor: S. R. Jain
Department: Aerospace Engineering

1. Introduction

Polymeric binders play a key role in solid composite propellants. Not only do they impart structural integrity to the propellant grain they also serve as fuels in the combustion process. Both the mechanical and combustion properties of the composite solid propellants are thus influenced by the polymeric binders used. The requirement of varied mechanical strength of the propellant grain to suit various missions is usually achieved by altering the binder characteristics, which often involves modification of the polymer backbone involving new synthesis. Production of new binders, however, is not only difficult but a costly affair. In this regard, the recent development in multicomponent polymeric systems offer exciting possibilities. In multicomponent systems involving blends, block and graft polymers or interpenetrating networks, it is possible at times, to achieve the desired properties, simply by changing the ratio of the components. Of the various systems cited, the interpenetrating polymer networks (IPNs)[1] offer several distinct advantages, and are expected to fulfill the stringent requirements as dense solid propellant binders. In view of this the present study is an attempt to synthesize and evaluate some of the promising IPNs as binders for solid composite propellants.

2. Experimental programme

Two component IPNs comprising polyurethane(PU)-poly(methylmethacrylate) (PMMA) and PU-polystyrens (PS) were prepared by the simultaneous polymerization process. The polyurethanes used are based on hydroxy-terminated polybutadiene(HTPB), and ISRO polyol(ISPO), a castor oil-based polyol developed by ISRO, India. The PU prepared by reacting with toluene diisocyanate(TDI) was crosslinked with glycerol, and the vinyl compounds, PMMA and PS, individually with divinyl benzene. Sixteen different IPNs were prepared by mixing each of the two polyurethanes (based on HTPB and ISPO) with each of the two vinyl monomers (MMA and styrene) taken in four different weight ratios. The IPN test samples were made by casting the mixture in a silicon oil-coated rectangular glass mould, and curing at elevated temperatures. The propellant samples were prepared by mixing ammonium perchlorate (AP) (70% by wt) powder of known particle size with the IPN mix and adding the curing agents subsequently. The propellant slurry was poured into aluminium moulds having teflon lining and cured for 72 h.

The newly synthesized IPNs were examined for their morphological, thermal and mechanical behaviour by scanning electron microscopy (SEM), simultaneous DTA-TG analysis and tensile testing, respectively. Other

physical properties such as viscosity, density and heat of combustion were also determined. The IPN-based propellants were examined for their structural strength and burning rates. A device was fabricated to determine the burning rate of the propellant strands at ambient pressure in controlled atmosphere.

3. Results and conclusions

The morphology of the IPNs, as revealed by SEM, clearly shows the typical characteristics of an interpenetrating structure. The vinyl phase is almost uniformly dispersed throughout the PU matrix. The formulation of IPN structure is vividly seen by the existence of intricate entanglements, wherein the polymer chain appears to penetrate inward and outward over one another in the matrix.

From the stress strain behaviour of the IPNs, it is evident that the tensile strength decreases initially as the amount of PU increases, reaching a minimum at 40% PU concentration and then again increases reaching a maximum at around 80% PU concentration. This behaviour is attributed to the plasticization effect of PU at the initial stage and increases in the crosslinks caused by interpenetration, at the later stage. The ISPO-based IPNs have lower tensile strength and higher elongation than those based on HTPB.

The viscosity of the prepolymer mixture decreases significantly with the addition of vinyl monomer. The actual densities of the IPNs are somewhat higher than those calculated, particularly, the PU-PS IPNs have significantly increased density. The increased density effects agree fairly well with the specific volume hypothesis[2]. The heats of combustion of IPNs based on HTPB are found to be higher than of those based on ISPO. The experimental values agree fairly well with those calculated by the method proposed by Jain[3].

The thermogravimetric data reveal the improved thermal stability of the IPNs. The weight retention of the IPN was found to be higher than the proportional average of the component networks when the PU concentration was 60–80%. The enhancement of the weight retention has been explained in terms of the unzipped monomers acting as scavengers for the radicals produced by the polyurethane degradation In general, the HTPB-based IPNs are more stable than those based on ISPO.

From the stress–strain data of the propellants processed at a constant level of solid loading using the IPNs as binders, it is observed that while the tensile strength increases, the percentage elongation at break decreases with increase in the concentration of the vinyl monomer. A variation in the ratio of the component polymers in the network results in composites having a wide range of mechanical strength. The burning rate data determined in the nitrogen atmosphere of the IPN-based propellants show that increasing the concentration of the vinyl components results in increasing the burning rate. The effect is more pronounced with PMMA–HTPB IPN systems. While ISPO-based polyurethane propellants do not sustain combustion, the ISRO-vinyl IPNS burn steadily, although the burning rates are much lower than those based on HTPB-vinyl IPNs.

In conclusion, the present work emphasises the advantage of IPNs as solid propellant binders. The IPNs are easy to synthesise and are capable of carrying high solid loading as required in composite propellants. Both the mechanical strength and burning rate of the propellant could be suitably modified as per the specific mission requirement by simply altering the constituent components or the composition of IPNs.

References

1. SPERLING, L. H. Interpenetrating polymer networks. In *Comprehensive polymer science*, Vol. 6 (Allen, G. and Bevington, J., eds), 1989, Pergamon.

2. KWEI, T. K., NISHI, T. AND ROBERTS, R. F. A study of compatible polymer mixtures, *Macromolecules*, 1974, **7**, 667–674.

3. JAIN, S. R. Energetics of propellants, fuels and explosives: a chemical valence approach, *Propellants Explosives Pyrotechnics*, 1987, **12**, 188–195.

Thesis Abstract (M.Sc. (Engng))

Characterization of copolyurethane networks as binders for solid propellants by V. Sekkar

Research supervisor: S. R. Jain
Department: Aerospace Engineering

1. Introduction

Polybutadiene binders have been extensively used in solid composite propellants. Not only do they give high specific impulse, but also their elastic nature imparts the desirable mechanical strength to the propellant grain. The requirement of mechanical properties of a propellant grain is, however, dictated by the structural load it is subjected to during combustion, flight and transportation Different applications thus demand different mechanical property requirements which are usually achieved by altering the polymer backbone, involving new synthesis. Production of the new polymers is an involved and expensive affair. The use of multicomponent polymer systems, on the other hand, offer attractive alternative, wherein it is possible at times, to achieve the desired properties simply by changing the ratio of the components and/or curing parameters.

Polyurethane networks especially those based on hydroxy-terminated polybutadiene[1] (HTPB) have been extensively used as binders for solid propellants. Networks based on ISRO polyol[2] (ISPO), an indigenously developed polyol by ISRO, India, have also been considered in recent years. Each of these systems has its own advantages. It is envisaged that the use of copolyurethanes based on these two prepolymers may possess the integrated benefits of the two binder systems, besides providing varied mechanical properties. In view of this the present study proposes the use of copolyurethanes based on HTPB and ISPO with various isocyanates, and reports a detailed investigation pertaining to their syntheses and characterization.

2. Experimental programme

The copolyurethanes were synthesized using four different ratios of HTPB and ISPO. The isocyanates used were, toluenediisocyante (TDI), hexamethylenediisocyanate (HMDI), polyanilinepolyisocyanate (PAPI) and isophoronediisocyanate (IPDI). The copolyurethanes were crosslinked using three different crosslinkers; trimethylolpropane (TMP), triethanolamine (TEA) and castor oil. In preparing the copolyurethanes the NCO/OH ratio was maintained at unity. A total number of 96 copolyurethane networks prepared were studied to evaluate the effect of composition, the isocyanate structure and the crosslinkers on the ultimate properties.

The copolyurethanes were characterized for their mechanical properties, such as tensile strength, modulus at 100% elongation, hardness and percentage elongation. The parameters like crosslink density and molecular weight between crosslinks were computed[3] from the polymer swell data. In a few cases, the dynamic mechanical analysis was carried out to ascertain the phase separation. The relative thermal stability of the copolyurethanes was examined using the thermogravimetric data.

3. Results and conclusions

The results provide ample evidence showing that copolyurethane networks differing widely in mechanical properties can be obtained by varying the component concentrations and other parameters. In general, the mechanical properties, such as tensile strength, modulus and hardness decrease on increasing the ISPO content of the copolyurethane, while the ultimate elongation increases. Copolyurethane structures made of aromatic isocyanates have better mechanical properties than those based on their aliphatic counterparts. The tensile strength, modulus and hardness could be increased by the use of crosslinkers. The relative effectiveness of the various crosslinkers varies in the decreasing order, TMP > TEA > castor oil. The use of crosslinkers usually causes a decrease in the percentage elongation.

Swelling studies reveal a close relationship between mechanical strength and crosslink density. The crosslink density of the copolyurethanes decreases with increase in ISPO content. Similarly, the relative

crosslink density achieved with the various trials follows a trend akin to that shown by the mechanical properties. In fact, almost linear plots are obtained when crosslink density is plotted against modulus, in some of these systems. The dynamic mechanical study shows the formation of random rather than block copolymers with no phase separation. The tan δ (max) of the copolyurethanes occur in between −60°C and −15°C, which are glass transition temperatures (tan δ (max), for HTPB and ISPO, respectively. The storage moduli data show that HTPB-based urethanes have lower moduli than those based on ISPO at temperatures below 0°C. The moduli values of the copolyurethanes lie in between those of the two individual urethanes. The viscosity build-up data show that the addition of ISPO to HTPB increases the gel time while curing with the isocyanates. Based on the rate of viscosity build-up the effectiveness of isocyanates follows the order, PAPI > HMDI > TDI > IDPI.

The thermal stability of the cured copolyurethanes depends on the specific type of the crosslinkers used. In general, the networks having higher amounts of HTPB are found to be more thermally stable. Of the various isocyanates HMDI appears to be most effective in imparting thermal stability to the polymer network. Irrespective of the type of crosslinker or chain extender used, however, the thermal stability of the copolyurethanes lies in between those based on the individual components, *i.e.*, HTPB and ISPO. The thermal stability of the polyurethanes also depends upon the crosslinkers used. Of the various crosslinkers, TMP imparts better thermal stability.

Overall, the study points to the wide scope of tailoring the mechanical properties of the polymer networks, often required in formulating the binder composition of solid propellants, simply by controlling the compositional and curing parameters.

References

1. BOYARS, C. AND KLAGER, K. — *Propellants manufacture–hazards and testing*, 1969, American Chemical Society.
2. KRISHNAMOORTY, V. N. AND THOMAS, S. — ISRO polyol—the versatile binder for composite solid propellants for launch vehicles and missiles, *Def. Sci. J.*, 1987, **37**, 29–37.
3. FLORY, P. J. — *Principles of polymer chemistry*, 1953, Cornell University.

Thesis Abstract (M.Sc. (Engng))

Flow visualization studies on transition and interaction of bubble plumes by Meheboob Alam

Research supervisor: V. H. Arakeri
Department: Mechanical Engineering

1. Introduction

A plume is a typical free shear flow which is characterized by a continuous source of buoyancy without any initial momentum. When a gas is released in the interior of an otherwise unconfined fluid (water), bubbles will form at the source and these rising bubbles along with the entrained fluid will form the '*bubble plume*'[1]. In an attempt to clarify some questions relating to the laminar–turbulent transition, we have performed a detailed flow visualization study of two-dimensional bubble-plume. In addition, interaction of a pair of equal strength two-dimensional bubble plume is also studied with the view that it might give us some idea regarding the entrainment of surrounding fluid.

2. Experimental methods

The plume is generated by a simple technique, 'electrolysis of water' from a line source. Since hydrogen bubbles are produced with much smaller size than the oxygen bubbles and at the same time volume of the hydrogen gas evolved is twice as much as that of the oxygen gas, only the cathode was used as the 'bubble generator'. The size of the bubbles obtained by this method ensured laminar flow over the bubble and this is an important aspect in view of transition study of the bubble plume. So, the hydrogen bubbles along with the entrained ambient fluid form the two-dimensional bubble plume.

To get an ideal line source, 'copper-clad laminate sheet' (generally used for PCB work) was found to be the best suited material for cathode. An array of seven cathode strips of width 1.7 mm with different aspect ratios was prepared on a copper-clad laminate sheet etching out the remaining copper part. The power supply and controls needed are simple. Basically it consists of a dc power source, a digital panel meter (DPM), a DPDT switch and variable resistances.

Experiments were performed in a glass tank of size $40 \times 40 \times 70$ cm with a free surface height of 50 cm. For transition studies one of the cathodes was switched on to the required current density by controlling the voltage on the 'dc power source' whereas two line sources of the cathode array were switched on at a time for interaction studies. From the measured instantaneous current, the gas flow rate was computed using Faraday's law. The plume was illuminated by a narrow sheet of light. The photographs were taken at an oblique angle using a 35-mm camera. The motor associated with the camera was used to take movie pictures.

3. Results and discussion

Some typical photographs are presented in Fig. 1 which display the effect of gas flow rate on transition height. Initially, the plume is straight followed by the appearance of small amplitude waves. These waves are amplified in the streamwise direction to reach unstable amplitude and then fold back to form discrete vortices. The arrow location in each photograph demarcates the transition into turbulent flow. It is evident that the increase in gas flow rate results in transition process occurring closer to the source.

The variation of transition height with aspect ratio and gas flow rate is shown in Fig. 2. The difference between the results for aspect ratios 25 and 50 proves one of the major facts in this type of flows; the two-dimensional free shear flows are more unstable than their axisymmetric counterparts[2]. Two-dimensionality of the flow field has been achieved at an aspect ratio of around 50 because there is no substantial difference in the transition data for aspect ratios of 50 and 100. Present experimental results are shown in Fig. 3 where non-dimensional transition height (X/D_0) is plotted against source Grashof number (Gr_D). Considering the fact that two-dimensionality has been achieved at an aspect ratio of 50, we have fitted a least square curve among all the data points for aspect ratios of 50 and 100. The corresponding 'asymptotic correlation' becomes

$$(X / D_0) = 1082.87 Gr_D^{0.0543}$$

FIG. 1. Sinuous instability of bubble plume: Qg (× 1000) = (a) 4.32, (b) 8.64, (c) 18.0 mm³/s/mm.

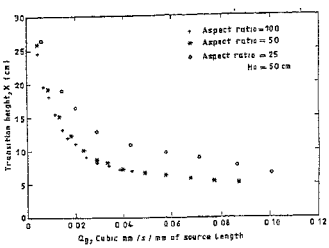

FIG. 2. Effect of aspect ratio and gas flow rate on transition height.

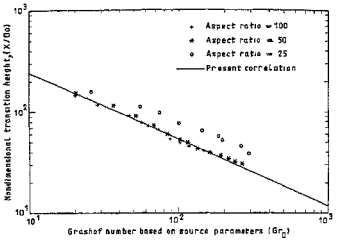

FIG. 3. Asymptotic correlation for a 2-D bubble plume.

4. Conclusions

For transition studies, disturbances were unambiguously antisymmetrical. Free surface effect was studied and it was shown that the transition height is not affected by the presence of free surface. Wave speed measurement from the photographs shows that the mean plume velocity is approximately twice the wave speed. An asymptotic correlation is given to correlate the transition height with corresponding source Grashof number (Gr_D).

Flow visualization of interaction between a pair of bubble plumes of equal strength revealed an important mechanism which states that the restriction in the entrained fluid is responsible for the downstream merging of the plumes. An approximate analysis was done which predicted a reasonable value of the entrainment coefficient (E = 0.025) for a two-dimensional laminar bubble plume.

References

1. LEITCH, A. M. BAINES, W. D. Liquid volume flux in a weak bubble plume, *J. Fluid Mech.*, 1989, **205**, 77–98.
2. GEBHART, B. *et al* *Buoyancy-induced flows and transport*, 1988, Hemisphere.

Thesis Abstract (M.Sc. (Engng))

Harmonic interactions in AC–DC systems due to converter transformer saturation

by M. M. Babu Narayanan

Research supervisors: K. R. Padiyar and S. Parameswaran
Department: Electrical Engineering

1. Introduction

By now, HVDC transmission is recognised as a viable alternative to AC transmission particularly for long-distance bulk power transmission, asynchronous interconnection between AC systems and underground or underwater transmission through cables. The integration of HVDC systems into existing large AC systems requires an understanding of the various AC/DC system interactions. Of the various types of AC/DC system interactions, the harmonic interactions can sometimes impair the satisfactory operation of a HVDC link unless suitable countermeasures are devised.

HVDC converters generate harmonics in AC currents. Under ideally balanced conditions, the AC currents of a 6-pulse converter bridge contain only harmonics of $6q \pm 1$ (q = 1,2...) which are commonly referred to as characteristic harmonics. It has been known that converters can also produce harmonics other than their characteristic harmonics under non-ideal operating conditions.

Besides converter, non-characteristic harmonics are also produced due to the nonlinear characteristics of the converter transformers. The presence of a direct current component in the transformer winding offsets the converter transformer flux to cause asymmetric or half-cycle saturation which injects a broad spectrum of harmonics into both the AC and DC sides. The reasons for the presence of a direct current in converter transformers are: 1) monopolar operation of HVDC systems resulting in ground currents entering the transformer neutral due to multiple parallel paths, 2) induction of fundamental frequency voltages on the DC lines, 3) firing pulse asymmetries, and 4) AC system transients[1,3]. Of these, the first two factors have been considered here for the investigations.

2. Model

The AC/HVDC system modelled for the studies is the national HVDC experimental line. This line links Lower Sileru in Andhra Pradesh and Barsur in Madhya Pradesh of the southern and western regions of India, respectively, transmitting DC power of 100 MW at + 100 kV in 6-pulse monopolar mode of operation with continuous ground return. A unique feature of this project is that the AC and DC power are transmitted on the same transmission tower[4].

3. Results and discussion

Power flow and transient stability studies were conducted for the test system. Power flow studies have been carried out taking into account the various system configurations. Of these, a configuration with an extreme 'strong' rectifier (Lower Sileru) with a short circuit ratio (SCR) of 40 and the 'weakest' inverter (Barsur) with an SCR of 4.5 was chosen for further investigations. Transient stability studies were conducted for the worst type of faults in the AC/HVDC system. Results show that there is a reduction in the DC power transfer during single-line-to-ground faults. However, the recovery of the DC system is fast, in about 100 milliseconds. Further investigations were carried out on the HVDC simulator.

The presence of a direct current in the transformer under monopolar operation of HVDC system was simulated by injecting a DC current through the neural of the converter transformer primary winding at the inverter end. Initially, under 1.0 pu power transfer, the injected current was varied in steps starting from 2.5% of the rated direct current (Id) to 20% of Id. Dynamic performance studies were also carried out to see the effect of DC injection on the fault recovery performance of the DC system. Studies were repeated for different DC power levels as also for different saturation level settings of the converter transformer. For one specific case of blocked converter conditions, analytical study results of converter transformer harmonic currents were obtained. It has been found that a near linear relationship exists between the converter transformer harmonic currents and the injected DC currents for lower values of DC injections. Steady-state operation of the HVDC system becomes difficult for values of DC injection of 10% of ID and for still higher values, the operation becomes impossible due to power oscillations and commutation failures. A comparison of the simulator study results with the field test results[5] and also the analytical study results is presented.

The effect due to the induction of fundamental frequency voltages on the DC line was investigated with particular reference to the control system interactions consequent on the saturation of converter transformer. The HVDC current controller parameters at the rectifier were changed in an interative manner for optimal performance under steady-state induction. Also, the effect of change in controller parameters on the harmonic point of view, the HVDC system performance is satisfactory if the induced 50 Hz voltage was below 15% of the rated DC voltage of reduction in harmonic levels on both AC and DC sides for reduced current controller gain settings. However, a reduction in gains beyond a certain limit has been found to result in poor fault recovery performance of the HVDC system.

4. Conclusions

The main conclusions of this study are:

1) A near linear relationship exists between the harmonics generated and the direct current in the converter transformer winding for low values of DC injection (up to 7.5% of Id). Beyond this, the harmonic currents increase rapidly.

2) Steady-state induction of fundamental frequency voltages into a HVDC line can lead to several adverse impacts on the HVDC system performance.

3) The major factors that govern the harmonic instability are: (i) the series impedance of the DC circuit, (ii) modulation of the delay angle by the current controller, and (iii) a weak AC system. The steady-state induction, which is an external phenomenon aids the first two factors to aggravate the original distortions.

References

1. YACAMINI, R. AND DE OLIVEIRA, J. C. — Harmonics produced by direct current in converter transformers *Proc. IEE*, 1978, **125**, 873–878.
2. NAKRA, H. L., LY X BUI, ISAO IYODA — System considerations in converting one circuit of a double circuit AC line to DC, *IEEE Trans.*, 1984, **PAS–103**, 3096–3103.
3. LARSEN, E. V., WALLING, R. A., AND BRIDENBAUGH, C. J. — Parallel AC/DC transmission lines steady-state induction issues, *IEEE Trans.*, 1989, **PD–4**, 667–673.
4. — National HVDC experimental line project (Lower Sileru–Barsur), Project report, 1987, BHARAT HEAVY ELECTRICALS LTD.
5. — Field test report on Lower Sileru–Barsur National HVDC experimental line commissioning tests, Barsur end, Technical report–723, 1991, CENTRAL POWER RESEARCH INSTITUTE, BANGALORE.

Thesis Abstract (M.Sc. (Engng))

Analysis of torsional interactions in AC and DC systems by M. K. Geetha

Research supervisor: K. R. Padiyar
Department: Electrical Engineering

1. Introduction

Series and shunt-compensated AC lines and HVDC transmission are used to meet the increasing demand of transmitting large blocks of power over long distances. Turbine generators connected to series-compensated lines can give rise to the phenomena of sub-synchronous resonance (SSR). Subsynchronous resonance is an electrical power system condition where the electrical network exchanges energy with the turbine generator at one or more of the natural frequencies of the combined system below the synchronous frequency of the system[1]. Subsynchronous frequency currents entering the generator terminal result in the generation of the voltages at the same frequency and it is possible that these voltages may sustain the currents to produce the effect that is called self-excitaztion. There are two types of self-excitation—one due to the induction generator effect and the other due to torsional interaction. The generator rotor oscillations at a torsional mode (of frequency f_m) induce armature voltage components of subsynchronous and supersynchronous frequencies given by

$$f_{em} = f_0 \pm f_m.$$

When f_{em} is close to an electrical resonance frequency f_{er}, ($f_{er} < f_o$) the phase angle of the voltage at this subsynchronous frequency is such as to sustain the torques at that frequency. The component of the torque in phase with the rotor velocity deviation (damping torque) is generally negative and if it exceeds the inherent

mechanical damping torque, the system will become self-excited. This interaction between the electrical and mechanical systems is called torsional interaction.

Torsional interactions can occur not only due to the series-compensated AC transmission, but also due to the presence of certain controllers in the system. For example, the torsional interactions can occur due to the speed input power system stabilizer (PSS) that are primarily used to damp the low frequency (< 2 Hz) rotor oscillations. The solution to this problem can be either in the form of providing a torsional filter or developing an alternate input signal for the PSS. The torsional interactions can also occur with current controller at the rectifier terminal of a HVDC link. The experience at Square Butte[2] indicated that HVDC systems could interact adversely with the torsional modes of vibration of an adjacent turbo-generator unit. It was found that when a turbine generator has a torsional mode whose frequency is within the bandwidth of HVDC current controllers, the torsional modes can be destabilized. Also, the interaction magnitude increases as the AC system in the vicinity gets weaker, resulting in maximum interaction for radial operation of DC system. The subsynchronous frequency oscillations can be stabilized by modifying the current controller loop.

Recent studies indicate that although fast-acting shunt compensation can be used to maintain voltage at appropriate points in the network by supplying or absorbing reactive power, unfavourable interaction can occur between a turbine-generator and static var compensator (SVC)[3].

2. Methods of analysis

The analysis of SSR and torsional interactions is usually carried out utilizing linearized models and system simulation. In the case of series-compensated AC lines, both eigenvalue analysis based on state space models[2] and approximate methods such as frequency scanning have been used. In the case of the HVDC link and SVC, self-excitation has been predicted based on the computation of electrical damping torques[3,5]. Eigenvalue analysis is also reported in Rostamkolai *et al.*[3] for a two-terminal DC link.

While there is extensive literature for the analysis of SSR in the series-compensated AC systems, there is not adequate coverage of the analysis of torsional interactions due to the presence of controllers such as PSS, HVDC converter and SVC control. The major aim of this work is to develop a general framework for the analysis of torsional interactions in AC and DC systems based on linearized state space model of the system. Eigenvalue analysis and system simulation for small perturbations are used to predict the small signal stability of the system. The methodology of developing the system model involves interconnecting the various subsystem models by identification of the interface variables. This approach permits flexibility in terms of additional controllers or subsystems and modifying the individual subsystem models. The component models include detailed modelling of generator, representation of AC and DC network transients and detailed representation of converters and controllers. The scope of the analysis is general enough to be applied to any system configuration.

3. Case studies

3.1. *Analysis with PSS*

The formulation of a linearized model of synchronous generator including AVR, PSS and torsional filter, and series-compensated AC line is carried out for the study of torsional interactions with PSS. The influence of the degree of series compensation on the stability of the system is studied by considering the IEEE first and second benchmark models. A PSS using speed input signal is designed to damp the low-frequency mode of the first benchmark model. Two countermeasures for damping the torsional modes are investigated. They are: (i) use of torsional filter with speed input signal, and (ii) using a combination of speed and acceleration as input signal. It is observed that the use of a control signal derived from speed and acceleration results in better damping of the critical torsional modes than the use of a torsional filter with speed input signal. Simulation is done for a step increase in the AVR reference input for the first benchmark model, with and without PSS. From the time response of shaft torques, rotor angle and electrical torque, it is seen that the torsional modes and also the low-frequency mode can be stabilized by proper choice of the parameters of PSS and torsional filter.

3.2. *Analysis with MTDC system*

A two-terminal DC system and three-terminal DC system are considered for case studies. For both the study systems, the sensitivity of various parameters such as the control mode and parameters at

each terminal and the location of the generator on the damping of torsional modes are investigated. Maximum interactions occur when the generator is at rectifier and with rectifier on current control. Also with rectifier operation as VST, the torsional modes are better damped.

For the two-terminal system with generator at inverter, the parameters of PSS (torsional filter considered) were so chosen as to damp the low frequency and also the torsional modes. For this case, simulation is carried out for a step change in the input of the voltage controller reference of the inverter. The time variations in shaft torques, rotor angle, DC currents and voltages following the disturbance are presented to evaluate the performance of the various controllers.

3.3. *Analysis with SVC*

The effect of the voltage controller gains of SVC on the damping of torsional interactions is studied. The study system consists of a generator feeding power to an infinite bus over a long transmission line, compensated at its midpoint by an SVC of the type fixed capacitor-thyristor-controlled reactor (FC-TCR). It is observed that for certain values of the integral controller gain of the voltage regulator, the torsional modes are negatively damped.

References

1. IEEE SSR TASK FORCE — Proposed terms and definitions for subsynchronous resonance in series compensated transmission system, *IEEE Trans.*, 1980, **PAS-92**, 506–511.
2. BAHRMAN, M., *et al.* — Experience with HVDC–turbine–generator torsional interactions at Square Butte, *IEEE Trans.*, 1980, **PAS-99**, 966–975
3. ROSTAMKOLAI, N., *et al.* — Subsynchronous torsional interactions with static compensators–Concepts and practical implications, Paper presented at *IEEE Summer Meeting*, Paper No. 89 SM 663-6, PWRS.
4. FOUAD, A. A. AND KHU, K. T. — Damping of torsional oscillations in power systems with series compensated lines, *IEEE Trans.*, 1978, **PAS-97**, 744–753.
5. KOTHARI, A. G. — *Analysis and simulation of HVDC turbine generator interactions*, Ph.D. Thesis, Indian Institute of Technology, Kanpur, India, 1985.

Thesis Abstract (M.Sc. (Engng))

A fault-tolerant transputer based firmware for parallel solution of partial differential equations by the boundary element method by R. Krishna Kumar

Research supervisor: S. K. Sinha
Department: Electrical Engineering

1. Introduction

Solution of partial differential equations (PDEs) is a compute-intensive task and parallel processing is being increasingly used for speeding up the solution of PDEs. Most of the reported schemes for the parallel solution of PDEs employ the finite difference method (FDM) or finite element method (FEM) on tightly coupled multiprocessor systems. The present study addresses itself to the parallel solution of PDEs by the boundary element method (BEM) on loosely coupled multiprocessor systems.

Transputers are well suited for building loosely coupled multiprocessors and a multi-transputer system has been chosen as the target hardware for the implementation of proposed parallel solutions of PDEs in the present work. The main motivation behind the present work has been the need to speed up the solution of PDEs of real-time applications. Since the reliability of the system is of paramount importance in real-time systems,

fault tolerant features have been included in the hardware. The resulting fault tolerant architecture can tolerate failure of any one component in the system.

2. Proposed parallel algorithms for BEM

Two parallel algorithms, named Par_inner and Par_outer, have been developed for solving single-zone two-dimensional PDEs by BEM. These algorithms have been implemented on linear arrays of transputers and tried for the parallel solution of Laplace equation. Par_outer has also been implemented on other topologies *viz.*, bi-directional ring and hypercube. The performance of the above implementation for different number of boundary elements and for different number of processing nodes has been studied. Par_outer has also been implemented on a linear array for the parallel solution of Poisson's equation.

3. The proposed fault-tolerant multi-transputer architecture

To improve the reliability of the system a new fault-tolerant multi-transputer architecture capable of tolerating failure of any one component in the system has also been proposed. The robustness of the fault-tolerant architecture has been thoroughly tested and proven by simulating faults during various stages in the execution of the proposed parallel algorithms. In the proposed fault-tolerant architecture the system is dynamically reconfigured on fault without requiring intervention from the human operator. After reconfiguration computations continue from the stage where the fault occurred. The process of reconfigurations is transparent to the user and the identity of the failed component is indicated to the user along with the results of the computations.

4. Results and discussion

The algorithms Par_inner and Par_outer were implemented on linear arrays of transputers for different number of nodes and Par_outer yielded better speed-ups compared to Par_inner. Par_outer was also implemented on ring and hypercube. However, the linear array yielded marginally better speed-ups compared to the ring and hypercube. The speed-ups increased nearly linearly with the number of processors and for Par_outer the speed-ups varied between a minimum of 1.91 for two processors and a maximum of 7.31 for nine processors on the linear array.

The robustness of the fault-tolerant architecture was tested by simulating faults during various stages of the execution of Par_outer and everytime the system returned the correct result. The degradation in computation time with faults occurring during the various stages of execution was also investigated. It was found that the fault-tolerant architecture provided graceful degradation depending on the stage at which the fault occurred.

The algorithms and the fault-tolerant architecture proposed in this study provide a framework for the development of a general-purpose firmware for the solution of PDEs by BEM which can be used in real-time applications.

References

1. ALBERTO, Z. AND SUBRATA, M. Vectorial and parallel processing in stress analysis by the boundary element method., *Int. J. Numerical Meth. Engng*, 1991, **31**, 307–317.

2. DAVIES, A. J. Quadratic isoparametric boundary elements: An implementation on the ICL DAP, *Boundary Elements-X*, 1986, **3**, 657–665.

3. DAS, P. K. AND FAY, D. Q. M. Dynamically reconfigurable multi-transputer systems, *Microprocessing Microprogm.*, 1988, **23**, 247–252.

Thesis Abstract (M.Sc. (Engng))

Internal partial discharge and breakdown characteristics of thin polypropylene films by R. Shobha

Research supervisor: R. S. Nema
Department: High Voltage Engineering

1. Introduction

Polypropylene (PP) film is being widely used as a dielectric in high-voltage capacitors. The design stress is of the order of 60V/μm. At this stress, one of the major causes of failure is partial discharges (PD). PD can occur in the cavities or gas pockets formed due to variation in the tightness of windings, improper impregnation and swelling of the film due to its interaction with the impregnating fluid. These cavities have a wide range of dimensions Although methods are devised to measure PD in insulation there is at present no standard method of estimating the life of insulation prone to PD. Moreover, it is not yet established which discharge quantity, out of maximum discharge magnitude, average discharge magnitude, total discharge magnitude and discharge energy, causes real damage leading to the difficulty in relating a discharge quantity and the life of insulation.

An attempt is made here to study the effect of cavity dimensions such as diameter (0.9 to 3.2 mm) and depth (40 to 200 μm on the various PD characteristics and the related breakdown and life of thin PP films.

2. Experimental

Electrical-grade biaxially oriented PP films of thickness 20 and 39.8 μm were cut as circular pieces of 11 cm diameter. Cavity was drilled in the 39.8 μm film at its centre using a high-speed PCB drilling machine. $2\pi/3$ Rogowski profile uniform field electrodes of 4.8-cm diameter (5.8-cm overall diameter) were used. The electrodes were embedded in epoxy except for the uniform field portion of the surface. The sample consisted of three layers, the top and bottom layer each of 20 μm in contact with the high voltage and ground and the middle layer with a cavity whose depth was varied.

A matching unit consisting of an RC circuit (R: 1500Ω, C:1000 pF), a coupling capacitor (600 pF, 30 kV), an amplifier (bandwidth 150 kHz), power frequency filter at the input and output of the amplifier, oscilloscope, and other necessary instruments were used for detection and measurement of discharges. The sensitivity of detection was 1 pc with a sample capacitance of 100 pF. Electronic counters were used for pulse height analysis.

To obtain the inception voltage, the voltage was increased to 50% of the expected value and held for 10 seconds. It was then increased gradually till discharge pulses just begin to appear. The voltage where pulses were continuous for 1 minute was considered as the inception voltage. Then voltage was gradually reduced till discharge pulses just disappeared to determine the extinction voltage. For studying the discharge characteristics, the voltage was maintained at 1.1 times of the inception and held constant for one hour. Measurements of maximum discharge magnitude and the pulse distribution were done at regular intervals of 4 minutes.

The breakdown characteristics of the samples were obtained by the step–stress method. The voltage was raised from 1000 V up to final failure of the sample in steps of 500 V, and held at each step for a finite time interval. The step–time intervals were 10, 5, and 3 minutes and 1 minute. The total time to failure was recorded using a microsplit second digital timer.

3. Results and discussion

The inception voltage increases with decreasing cavity diameter for a given depth and increasing cavity depth for a given diameter. Initial (first) measurement for inception gives the highest value for inception and subsequent measurements show a reduction in the inception voltage leading to a stabilization at a specific value. This stabilized value, V_i, bears a definite relation with the diameter and depth of the cavity (Fig. 1) and is given by $V_i = A(d/t')^{-B}$ where A and B are constants, d, the cavity diameter, t', the cavity depth. The extinction voltages are 12 to 20% lower than the inception value.

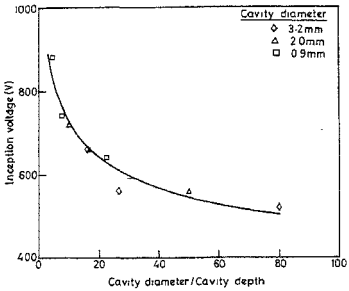

FIG. 1. Variation of inception voltage (stabilized) with cavity diameter/depth.

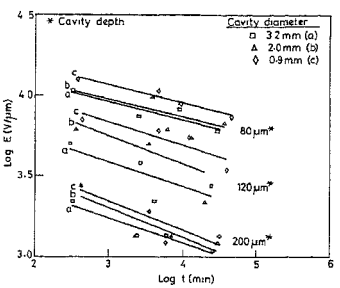

FIG. 2. Effect of cavity dimensions on the E-t characteristics.

The accumulative repetition rate against apparent charge shows an exponential distribution as compared to an ideal rectangular distribution[1]. Measurements indicate that a single discharge does not completely discharge the entire cavity. The discharge pulse magnitudes and their distribution opened on the diameter as well as depth of the cavity. The total discharge quantity increases with increasing diameter as well as depth of quantities (maximum, total and average magnitudes and number of pulses/second) is less in a smaller diameter cavity.

The inverse power-law model has been frequently used to estimate lifetimes of insulating materials under voltage stress. In the simplest form, this model is represented by the equation

$$t(E)^n = K \tag{1}$$

where t is the time to failure at voltage stress E, n and k are constants. Starr and Endicott[2] proposed the concept of equivalent damage to estimate the life at constant stress from that on linearly increasing progressive stress. They found that the data fit a straight line on a log–log paper for progressive stress and hence suggested the applicability of inverse power–law model for progressive stress also. Assuming a similar cumulative nature of damage to the insulation for the step–stress, the cumulative damage will be the sum of the damages at each voltage level, given by

$$t(E)^n = \sum_i t_S(E_S)^n + t_{S+1}(E_{S+1})^n \tag{2}$$

$t_i E_i$ is a product of time and voltage stress at each fully completed step and t_{s+1} is the time to failure on the uncompleted t_{s+1} step. Comparison of eqns (1) and (2) indicate that the right hand side of eqn (2) is a constant and is independent of the time interval t_2 chosen provided the ageing mechanism has not changed over the covered range[3].

The breakdown stress against time to failure, E-t characteristics, is shown in Fig. 2. The n values obtained from these curves as well as the k values computed using the step–stress data are tabulated in Table I. n values decrease with increase in cavity depth and the discharge quantities very with varying cavity dimensions. An attempt has been made to fit an equation of the form $n = A' \exp(-B' Q_m)$, where A' and B' are constants and Q_m, this maximum discharge magnitude. On extrapolation, this equation gives an 'n' value of 11.3 for a permissible discharge magnitude of 10 pc. Krishnan and Nema[4] in their work on surface PD ageing of PP films have obtained n value corresponding to 10 pc as 11.8. The total discharge quantity/second (Q_t) up to failure correlates with the time to failure (L) in the form $L = a(Q_t)^{-b}$ (Fig. 3). This indicates that Q_t seems to be

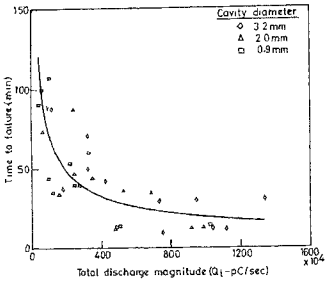

FIG. 3. Variation of time to failure with total discharge magnitude.

an important factor in the degradation of PP films. This aspect falls in line with the observations of Krishnan and Nema[4] where a similar relation for L and Q, is obtained for surface discharge studies, and also of Dakin[5] where it is stated that the rate of material degradation is proportional to the total number of discharges per second. Also, it is found that for a given diameter and depth of the cavity the k values corresponding to 10, 5, and 3 minutes and 1 minute step–time are all of the same order. Therefore, the step–stress method can be used for a quick determination of the constants of the inverse power–law model for life characteristics.

Table I Constants n and k of the inverse power–law model

		Cavity diameter (mm)		
		0.9	2.0	3.2
Cavity depth: 80μm				
	n	9.02	9.23	8.88
	k	2.2×10^{15}	3.55×10^{16}	6.23×10^{15}
Cavity depth 120μm				
	n	7.03	5.99	6.60
	k	1.36×10^{12}	5.20×10^{10}	7.21×10^{10}
Cavity depth: 200μm				
	n	5.59	5.53	6.5
	k	4.68×10^{8}	6.79×10^{9}	2.49×10^{9}

k: Average of K_{10}, K_5, K_3, K_1 calculated using step–stress data.

References

1. TANAKA, T. AND IKEDA, Y. — Internal discharges in polyethylene with an artificial cavity, *IEEE Trans.*, 1971, **PAS-90**, 2692–2702.
2. STARR, W. T. AND ENDICOTT, H. S. — Progressive stresses–A new accelerated approach to endurance, *AIEE Trans.*, 1961, **PAS-80**, 515–523.
3. LAGHARI, J. R., CYGAN, P. AND KHECHEN, W. — A short method of estimating lifetime of polypropylene film using step–stress tests, *IEE Trans.*, 1990, **EI-25**, 1180–1182.
4. KRISHNAN, V AND NEMA, R. S. — A study of short-term partial discharge ageing of polypropylene film, *IEEE Trans.*, 1989, **EI-24**, 1133–1140.
5. DAKIN, T. W. — Theory of voltage endurance, Addendum to *Conf. Proc. CEIDP*, 1984, pp. 1–6.

Thesis Abstract (Ph.D.)

Temperature programmed desorption studies of some heterogeneous catalytic processes by M. Jayamurthy

Research supervisor: S. Vasudevan
Department: Inorganic and Physical Chemistry

1. Introduction

The key to understanding any heterogeneous catalytic process lies in the identification of the primary rate determining steps. The study describes how temperature programmed desorption (TPD), under reactive and non-reactive conditions can be used as a probe to achieve this. Three heterogeneous catalytic processes have been studied using this technique. They are: i) the conversion of methanol to gasoline (MTG) over ZSM–5, ii) Hydrodesulphurization (HDS) of thiophene over a series of Co–Mo/γ–Al_2O_3 catalysts, and iii) the effect of 'strong metal support interaction' (SMSI) on the hydrogenolysis of cyclohexane over Rh/TiO_2.

2. Results and discussion

Temperature programmed desorption is a simple technique which has been widely used both in surface science as well as in heterogeneous catalysis. In this technique the desorption of a preadsorbed gas from a catalyst surface, is measured as a function of a programmed temperature rise, so that the rate of desorption as a function of temperature is obtained. The technique yields information on the nature and strength of the interaction between the desorbing species and the surface in the adsorbed state, as well as on the multiplicity of adsorption sites. If the experimental conditions are such that, apart from the simple desorption process, reactions can also take place, then it can give both qualitative as well as quantitative information on the kinteic parameters for various reaction steps. The latter technique has been called 'temperature programmed surface reaction' (TPSR). A combination of TPD and TPSR experiments can help in identifying the various steps involved in a heterogeneous catalytic process and the determination of the associated activation barriers.

In the present study, the experimental set-up consists of two main components: i) a reactor whose temperature can be programmed and ii) a detector. The experiments have been studied in a flow of inert gas or a reactive gas in TPSR experiments. The detector was a quadrupolar mass spectrometer. The data were analyzed assuming that the desorption rate could be described by an Arrhenius (or Polanyi–Wigner) equation[1].

$$-d\theta / dt = k_d . \theta^n = \theta^{\exp[-E^*/RT]}\theta^n$$

The desorption profiles were derived from the mass balance equations. The rate equations for various desorption profiles were derived. The final form of the equations for various situations is as follows.

1. First order without readsorption

$$\ln[C_n] = x - \exp[x] / (1 - x / E_m)^2 dx \qquad (1)$$

2. First order with readsorption

$$C_n = (\theta / 1 - \theta)\,(1 - \theta_m) / \theta_m \exp[x] \qquad (2)$$

3. Second order without readsorption

$$C_n = (\theta / \theta_m)^2 \exp[x] \qquad (3)$$

4. Second order with readsorption

$$C_n = \frac{\theta^2}{(1-\theta)^2} \frac{(1-\theta_m)^2}{\theta_m^2} \exp[x] \qquad (4)$$

The kinetic parameters were extracted from the experimental desorption profile by curve fitting the data on the theoretical expressions for the rate of desorption.

The method developed is applied for the study of the conversion of methanol to gasoline (MTG) over the high silica synthetic zeolite – ZSM–5. This process has been the subject of numerous NMR and IR spectroscopic studies[2,3]. The TPD of methanol from H–ZSM–5 for various coverages have been studied. The TPD experiments are clearly able to identify the primary steps and follow the progress of the MTG process. The two steps are: 1) the dehydration of CH_3OH to dimethylether (DME) and 2) the conversion of dimethylether to hydrocarbons.

The importance of the Bronsted acidity of the zeolite in the MTG process was clearly established. It was found that more than one methanol was absorbed on these sites (a protonated cluster) with a spectrum of desorption energies corresponding to the process $(CH_3OH)_nH^+–Z^- \rightarrow (CH_3OH)_{n-1}H^+–Z^- + CH_3OH$. The desorption energy decreases with increasing n. For the second step, too, these sites are important. The activation barriers for the two steps were obtained by curve fitting the product profiles to theoretical expressions. A comparison of thermodynamic and kinetic parameters of the catalytic process with the corresponding 'gas phase' ion-molecule reaction[4] was made.

The hydrodesulphurization (HDS) process over Co–Mo/γ–Al_2O_3 catalysts is one of the most widely practised industrial reactions. The role of Co, however, still remains enigmatic[5]. The desorption (TPD) as well as the reaction (TPSR) of thiophene have been studied over a series of Co-Mo/γ-Al_2O_3 catalysts. The objective of the present work was to understand how Co promotes the HDS activity. As part of the study, the desorption (TPD) as well as reactions (TPSR) of some key C_4 hydrocarbons, which have been implicated by various mechanistic proposals, were examined. The hydrocarbons studied were butane, butene and butadiene.

The desorption experiments of the hydrocarbons over sulphided catalysts, with and without Co, showed that the introduction of Co makes a new site available for adsorption, while at the same time, the site on the 'Mo–S' component of the catalysts remains unaffected. Reaction of hydrocarbons absorbed on the two sites appears to proceed independent of each other and no promotion by Co was observed.

One of the surprising features of the present study was the fact that the presence of Co does not affect the absorption sites for thiophene. TPD profiles of thiophene over a series of sulphided Co–Mo/γ-Al_2O_3 catalysts were almost identical. When the desorption experiments were done using H_2 as a carrier gas (TPSR) then in addition to thiophene, the evolution of the desulphurized products were also observed. For all catalyst combinations, the products observed were butane and butene. Neither the evolution of butadiene nor the hydrothiophenes were observed. The kinetic parameters for the HDS reactions were obtained by curve fitting to the relevant rate expressions. It was found that the presence of Co brings down the activation barrier as well as the temperature of the HDS reactions.

A comparative study of the hydrogenolysis of cyclohexane over 2% Rh/TiO_2 catalyst in the normal state (low temperature reduced) and in high temperature reduced state where the catalysts exhibit the so-called 'strong metal support interaction' (SMSI) effect was carried out. It was found that the TPD techniques were unsuitable in the present case since the rates for desorption and reaction were much lower than the experimentally realizable rates of heating. The possibility of using a pulse technique[6] for determining the rate constants is explored. The conditions under which the pulse technique can yield the rate of desorption or reaction are described. It was found that the catalysts in the SMSI states had a higher activation barrier for hydrogenolysis but at the same time the heats of desorption for all the catalysts are identical. This implies that the difference in the activity is not due to a modification of adsorption sites for cyclohexane adsorption.

References

1. HENSEN, R. S. AND MIMEAULT, V. S. — In *Experimental technique in catalytic research* (Anderson, R. B., ed.) 1967, p. 220, Academic.
2. CHANG, C. D. AND SILVESTRI, A. J. — *J. Catal.*, 1977, **47**, 249–259.
3. ANDERSON, M. W. AND KLINOWSKI, J. — *J. Am. Chem. Soc.*, 1990, **122**, 10–16.
4. BASS, L. M., CATES, R. D., JARROLD, M. F., KIRCHNER, N. J. AND BOWERS, M. T. — *J. Am. Chem. Soc.*, 1983, **105**, 7024–7033.

5. PRINS, R., DE BEER, V. H. S. AND SOMORJAI, G. A. *Catal. Rev.–Sci. Engng*, 1989, **31**, 1–41.

6. GIDDINGS, J. C. *Dynamics of chromatography*, Part 1, *Principles and theory*, (Ch. 2), 1965, Dekker.

Thesis Abstract (Ph.D.)

A study of a class of water wave scattering problems by L. Vijaya Bharathi

Research supervisor: A. Chakrabarti
Department: Mathematics

1. Introduction

The problems of scattering of surface water waves by barriers bearing several geometrical shapes (within the framework of linearized theory) reduces to a class of mixed boundary value problems (BVP) associated with Laplace's equation for the determination of the velocity potential. A number of such BVPs is studied in the present work by using the techniques of Green's function-cum-integral equation approach as well as the complex variable methods involving Riemann–Hilbert problems.

2. Problems solved and methods used

The two basic problems of water wave scattering associated with a surface piercing and a submerged vertical barrier have been solved using a new Green's function method. The Green's function associated with the BVPs is rederived using a Fourier integral transform technique involving a mixed trigonometric Kernel. Employing Green's second identity along with this new Green's function, two integral equations for the 'jump' and the 'sum' of the limiting values of velocity potential across the barrier are derived. The solutions of these integral equations are obtained by using various properties of the integral transform used. The equivalence of various representations of the velocity potential is established and known results associated with reflection and transmission coefficients (R&T) are derived.

In the use of the complex variable method, the mixed BVP associated with the Laplace's equation is converted to the problem of solving a sectionally analytic function satisfying certain boundary conditions (BC) on cuts following the established procedure involving complex potentials and the utility of Schwarz's reflection principle. The problem is then solved by deriving two uncoupled Riemann–Hilbert problems for two new sectionally analytic functions. The solutions of these problems are then used to obtain the velocity potential using the contour integration methods.

This new technique is employed to solve the problem of a submerged vertical barrier with a gap in between. The R&T and the near field are obtained by employing the contour integration procedures. A limiting case is shown to produce the established results. The numerical results in the form of graphs for various limiting cases are compared with those of the established ones.

The problems associated with nearly vertical barriers of different geometry and shapes are also solved using this new complex function techniques. Following the earlier workers the problems under consideration are converted into 2 BVPs assuming a perturbational series expansion for the velocity potentials. The solution of one BVP is well known and the other BVP for Laplace's equation is different from the ones encountered earlier because of the fact that the BCs on the barrier to be satisfied by the potential function are two different known functions for the two approaches, from the left and from the right, respectively. The solution of this new BVP is obtained (for the first time) using the complex variable technique and the constants R_1 and T_1 representing the first-order corrections to the reflection and transmission coefficients are obtained. The near field is also derived in all the three cases. Using the established result $T_1 = 0$, the value of R_1 is rederived and a new identity to be satisfied by the shape function defining the barrier is obtained.

A new method is described for tackking certain Dirichlet-type BVP in two dimensions for a plane cut along a circular arc. The problem is then solved by using the properties of inverse points with respect to a circle, following a similar method as in the above problems. The solutions are compared with those obtained by the singular integral equations approach. The present analysis simplifies the integral equation approach to a large extent. Thus the method which is a generalized version of the one used in earlier problems show that *wider* applications to the problems associated with smooth cuts of arbitrary shapes are possible.

Following this above general approach the problem of scattering of water waves by a circular-arc-shaped barrier is solved. The coefficients of R and T as well as the near field are obtained. For various particular positions of the circular-arc-shaped barrier the numerical values of |R| and |T| are presented in tabular forms.

3. Conclusions

Two different types of methods, *viz.*, (i) the Green's function-cum-integral equation method, and (ii) the complex variable method, have been further developed and utilized in a variety of scattering problems in the linearized theory of water waves. Known results have been rederived by using some of the results of more general scattering problems discussed in the work under certain special limiting conditions.

References

1. VIJAYA BHARATHI, L. AND CHAKRABARTI A , A Solution of a boundary value problem associated with diffraction of water waves by a nearly vertical barrier., *IMA J. Appl. Math.*, 1991, **47**, 23–32.
2. CHAKRABARTI, A. AND VIJAYA BHARATHI, L. Transmission of water waves through a gap in a submerged vertical barrier, *Indian J. Pure Appl. Math*, 1991, **22**, 491–512.
3. CHAKRABARTI, A. AND VIJAYA BHARATHI, A. A new approach to the problem of scattering of water waves by vertical barriers, *ZAMM*, 1992, **72**, 415–423.
4. VIJAYA BHARATHI, L., CHAKRABARTI, A., MANDAL, B. N. AND BANERJEA, S. Solution of the problem of scattering of water waves by a nearly vertical plate, *J. Aust. Math. Soc., B.*, 1994, **35**, 382-395.

Thesis Abstract (Ph.D.)

Investigations on the mechanical threshold in IV–V–VI glasses by A. Srinivasan

Research supervisors: E. S. Raja Gopal and V. Sasisekharan
Department: Physics

1. Introduction

The chemically ordered covalent network (COCN) model[1] and the rigidity percolation (or Phillips and Thorpe) model[2] attempt to predict the composition dependence in chalcogenide glasses. According to the COCN model, glasses with stoichiometric compositions are more chemically ordered than the others. These compositions are referred to as the chemical threshold of the particular family of glasses.

The Phillips and Thorpe model views the changes in the glassy network in terms of the average coordination number $<r> = <r>_c = 2.40$. The glasses with $<r> < <r>_c$ are 'floppy' and the glasses with $<r> > <r>_c$ are 'rigid'. At $<r> = <r>_c$, a transition from a 'floppy' to 'rigid' glass occurs. $<r>_c$

is also referred to as the rigidity percolation threshold. Lately, Tanaka's argument[3] based on medium range interactions existing in hese glassy networks, suggest that the mechanical threshold occurs at $<r>=<r>_c=2.67$. There is a general lack of consensus in the literature about the correct value of $<r>_c$ in chalcogenide glasses. It is also not clear whether the mechanical or chemical model is more appropriate for interpreting the composition-dependent properties of chalcogenide glasses. The present investigations on IV–V–VI glasses was taken up to clarify these points.

2. Experimental

Two sets of Ge–Sb–Se, Ge–As–Te and Si–As–Te glasses were prepared using the melt-quenching technique. The glass compositions were chosen to cover the $<r>$ range $2.30 \leq <r> \leq 2.75$, so that both the $<r>$ values in question, namely, 2.40 and 2.67, were covered.

Differential scanning calorimetry (DSC) has been used to determine the glass transition temperature (T_g), crystallization temperatures, melting temperature and the activation energy of crystallization (E_c) of the glasses. The DSC experiments were performed on a commercial Stanton Redcroft DSC 1500 system. Photoacoustic (PA) experiments pertaining to the determination of the optical band gap (E_o) and thermal diffusivity were performed on a locally assembled PA spectrometer[4]. High-pressure resistivity studies have been performed on the Ge–As–Te and Si–As–Te glasses using a 6-mm calibrated Bridgman anvil apparatus.

3. Results and discussion

3.1. *PA studies*

E_O of the two sets of Ge–Sb–Se glasses show a maximum at $<r>=2.60$ (Fig. 1a). The E_O *versus* $<r>$ plots for *the two sets of Ge–As–Te and Si–As–Te glasses saturate after* $<r>=2.60$. The α versus $<r>$ *plots for the two* sets of Ge–Sb–Se, Ge–As–Te (Fig. 1b) and Si–As–Te glasses consistently show at $<r>=2.60$. The PA studies, however, show no observable anomaly at $<r>=2.40$. The results suggest that a mechanical threshold occurs at $<r>=2.60$ as suggested by Tanaka[3]. Tanaka's estimate of the threshold at $<r>=2.67$ is based on pure covalent bonding. Elements like Sb and Te with non-covalent bonding character, could be responsible for the observed shift in the threshold values.

3.2. *High-pressure studies*

The pressure derivative of the logarithm of the normalized resistivity, namely, $d[\log(R/R_O)]/dp$ (where R/R_O is the normalized resistivity and P, the pressure) of the two sets of Ge–As–Te and Si–As–Te (Fig. 2a) glasses at low pressures (up to 1.5 GPa) show a minimum at $<r>=2.60$. A minimum in $d[\log(R/R_O)]/dp$ signifies a minimum response to applied pressure, a typical characteristic of a glass at the rigidity percolation threshold. The earlier reports[3] on various properties of Ge–As–S glasses show anomaly near $<r>=2.67$, which is quite consistent with the above observations.

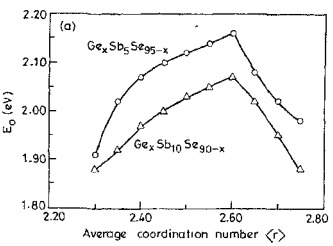

FIG. 1 a.

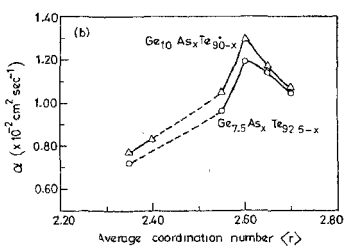

FIG. 1 b.

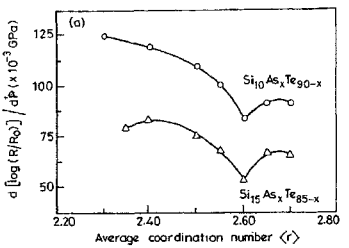

FIG. 2 a.

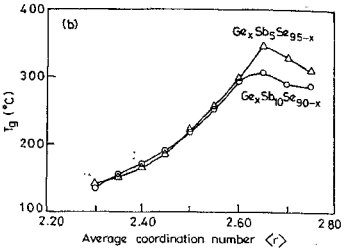

FIG 2 b.

3.3. *DSC studies*

The T_g *versus* $<r>$ data for the two sets of Ge–Sb–Se glasses (Fig. 2b) are dependent only on $<r>$ up to $<r> = 2.60$, which supports the PA and high-pressure results obtained for this glass system.

However, the composition dependence of the activation energy of the first (and second) crystallization (E_{c1} and E_{c2}) of the two sets of Ge–Sb–Se, Ge–As–Te and Si–As–Te glasses show a maximum near the stoichiometric compositions. This shows that E_c is more sensitive to the chemical ordering occurring near the chemical threshold.

4. Conclusions

The PA and high-pressure resistivity studies on three glass systems belonging to IV–V–VI group of chalcogenide glasses show anomaly at $<r> = 2.60$, which is close to Tanaka's $<r>_c$. The E_c of the three glass systems show anomaly near their respective chemical thresholds. Thus, both the chemical and the mechanical thresholds are observed in these studies. The relative sensitivity of the physical property to the state of the local ordering appears to be crucial in determining the correct model (COCN or rigidity percolation) for interpreting the results of such studies.

References

1. LUCOVSKY, G. AND HAYES, T. M. — Short-range order in amorphous semiconductors. In *Amorphous semiconductors*, (M. H. Brodsky, ed.), 218, 1979, Springer Verlag.
2. PHILLIPS, J. C. AND THORPE, M. F. — Constraint theory, vector percolation and glass formation, *Solid State Commun.*, 1985, **53**, 699–702 (and the references quoted therein).
3. TANAKA, K. — Structural phase transitions in chalcogenide glasses, *Phys. Rev. B*, 1989, **39**, 1270–1279.
4. MADHUSOODANAN, K. N., PHILIP, J., PARTHASARATHY, G., ASOKAN, S. AND GOPAL, E. S. R. — Optical absorption and thermal diffusivity in Ge_xTe 100-x glasses by the photoacoustic technique, *Phil. Mag. B*, 1988, **58**, 123–132.

Thesis Abstract (Ph.D.)

An investigation into the phenomena of the growth of electrical trees in PMMA by B. Prathap

Research supervisors: V. Prabhashanker, R. S. Nema and G. R. Nagabhushana
Department: High Voltage Engineering

1. Introduction

Though the breakdown of electrical insulation appears to be catastrophic in nature, it is preceded by the growth of fine hollow, often carbonized, microscopic channels in the form of trees[1]. These trees originate at locations of high stress concentration and proceed in the direction of the field and manifest as electrical, water or electrochemical trees depending on the environment of occurrence. Electrical tree growth is associated with occurrence of partial discharges (PDs). Earlier attempts to correlate PDs with tree growth have not been successful since trees can continue to grow with very small discharges even after substantial tree growth has occurred. The variation of space charges with time are complicated and it is very difficult to associate level of applied voltage with PDs measured. Hence, a whole set of PDs has been considered and the properties of the set have been associated with type and growth of the trees. A statistical analysis of the data has been made to understand the characteristics of the PD data associated with tree growth.

Literature indicates that the tubules from the pathways of breakdown and the trapped charges play an important role in causing the spatial randomness of the trees. An electrostatic field stimulation of tree tubules has been made to get a quantitative picture of the fields around the tubules, as they grow during ageing, to predict the future growth of the channels.

2. Experimental procedure

PMMA (Polymethyl-methacrylate) samples with embedded gramophone needles forming a point-plane gap of 3 mm were aged with 50 Hz ac voltage at 1.25 times the partial discharge inception voltage. Generally the ageing voltage ranged between 15 and 20kV; bush-type trees requiring higher inception voltage as compared to the branch type. This ageing was simultaneously monitored by collection of PDs at regular intervals of time for a mixed duration and periodic microphotographing of the tree. The sequential pulse amplitude records were converted to frequency tables using the earlier noted attenuation and amplifications. Such PD pulse amplitude records were tested for different distributions and it was found that a 2-parameter Weibull distribution was sufficient to represent the data in all cases. The parameters of the distributions along with their total number of pulses were accumulated in a data file. Such a data file was further analyzed using time and frequency domain 'time series analysis' methods.

3. Statistical analysis of partial discharge data

The PD pulse amplitude records obtained during ageing were converted to frequency distributions using the earlier noted amplifications and the system calibrations. Nearly 1000 pulse amplitude distributions were tested with several continuous statistical distributions. It was found that a two-parameter Weibull distribution could represent the data for both bush- and branch-type trees. The cumulative distribution function of the two-parameter Weibull distribution is given by

$$F(q_i) = 1 - \exp(-(q_i / \sigma)^{\eta})$$

where $F(q_i)$ is the cumulative probability of 'q' being less than or equal to 'q_i' σ, the scale parameter (63.2 percentile) and η, the shape parameter.

The possibility of relating the discharge magnitude distribution with ageing time 't' was examined by 'time series analysis' of the variations of a σ and η with 't' in time and frequency domains.

The σ time series can be decomposed into 'deterministic' and 'stochastic' portions as follows.

$$\sigma(t) = \sigma_d(t) + \sigma_r(t)$$

where $\sigma_d(t) = a_0 + a_1 t + a_2 t^2$

and a_0, a_1 and a_2 are the coefficients of a second degree polynomial. It can be seen that $\sigma_d(t)$ for the branch-type tree is higher and increases steadily with a higher rate of rise. In the case of bush-type, $\sigma_d(t)$ is lower, has lesser rate of rise increase initially but decreases later.

The 'n' time series can be decomposed into deterministic and stochastic portions as follows.

$$\eta(t) = \eta_d(t) + \eta_r(t)$$

$$\eta_d(t) = 1/N \sum_{i=1}^{N} \eta(t_i)$$

and N = no. of data points.

Correlation and spectral analyses of the data has been made using standard algorithms[2]. The auto and cross correlations for σ_r and η_r are determined. A second-order autoregressive (AR) model sufficiently describes σ_r and η_r for both bush- and branch-type trees as shown below.

$$\sigma_r(t) = \sum_{u=1}^{p} \phi_u \sigma_r(t-u) + a_t \text{ where } 0 < p < 2$$

$$\eta_r(t) = \sum_{u=1}^{p} \psi_u \eta_r(t-u) + b_t \text{ where } 0 < p < 2$$

where ϕ and Ψ are the AR parameters of the model whose roots lie within the unit circle conforming to a stable linear system. From the above equations it can be seen that, at any instant t the value of either $\sigma_r(t)$ or $\eta_r(t)$ can be represented as a function of its own past values at t-1, t-2, respectively.

The autospectra of σ_r and η_r are dominated by low-frequency components but the high-frequency amplitudes for the bush are higher than those of branch. Cross-correlations, all of one sign, produce low-frequency cross-amplitude spectra while oscillatory cross-correlations produce high-frequency cross-amplitude spectra. The analyses indicated that the system exhibits a memory-based mode, where the past values influence the future values.

The results could be explained by a physical model. The surface charges and the main field charges (electrons and ions) will penetrate ahead or adjacent to the tubule, altering the field accordingly, forming a branch- or bush-type of tree. Thus in the branch-type tree, bubbles grow in progression giving rise to a high value of σ_d which rapidly grow as ageing proceeds. With the bush type, after each tubule is created more will be created of the same type as defined by σ_d. Then the next level could be covered giving rise to a slower rate of rise of σ_d with ageing time t. If the material is homogeneous with respect of breakdown strength then the adjacent tubule growth would be encouraged as opposed to the case where large inhomogeneity is found along the field direction which encourages branch growth. This is evidenced by higher value of η_d and inception voltage for bush-type tree as compared to branch type. Since η_d is independent of σ_d, η_d may be considered to indicate the level of homogeneity of the material and, σ_d the magnitude of the unit tubule length.

4. Field simulation

As the tree growth showed spatial randomness, a field simulation using charge simulation method[3] to simulate needle-plane and the tubule-image systems was adopted to predict the future growth of the trees. Of the several PMMA samples aged, one was selected and the microphotographs were taken at different sections. A photograph was selected in which edges of breakdown paths starting from the electrode and the needle contour were clearly defined, such that the discharge paths considered for study would be in a plane passing through the axis of the needle.

Two series of simulation studies were carried out. In the first, the potential plots were obtained. These plots gave a qualitative idea of the potential and stress distribution at the areas of interest. A detailed examination of the plots showed that the presence of the tubules alters substantially the main field and the introduction of fresh tubules alters the earlier combined potential fields. In any particular area of interest, the sequence in which the tubules appear affects the potential distribution substantially. In a practical 3D system, the total stress at the starting points on the tubule surface as well as along the field line will largely determine the direction of future growth. The stress lines starting from selected points on tubule surfaces along three planes were considered and detailed analysis was made. A few points on tubule surfaces were selected from the critical areas. Parameters such as stresses at the starting points of the field line, modification of the ratios of total stresses along the field line, to the total stresses at the first point and the location of the point of maximum stress were all determined taking one tubule at a time, two tubules at a time and in the presence of all the three.

The analysis of the results of the simulation showed that the growth of a channel at any point can be predicted knowing the sequence in which tubules occur. The possibility of discharges occurring ahead or adjacent to a tubule would help in fixing the shape of the tree.

References

1. McMahon, E J. — A tutorial on treeing, *IEEE Trans.*, 1977, **EI-1**, 277-288.
2. Box, G. E. P. and Jenkins, G. M. — *Time series analysis: Forecasting and control*, 1976, Holden Day.
3. Singer, H., Steinbigler, H., and Weiss, P. — A charge simulation method for the calculation of high voltage fields, *IEEE Trans.*, 1974, **PAS-93**, 1660–1668.

Thesis Abstract (Ph.D.)

Fast transient voltage distribution in HVDC converter valves cascaded with converter transformer and reactor by S. Rajasekharaiah

Research supervisor: H. S. Chandrasekharaiah
Department: High Voltage Engineering

1. Introduction

HVDC power transmission, having been attempted as a successful complement to its AC counterpart, is still a challenge to the power engineer because of its complex behaviour and complicated network topology. The nature of complexity assumes different dimensions during steady and transient states of operations under identical system configurations. A study of the system behaviour under fast transient conditions is of greater importance as it determines the maximum stresses experienced by the converter modules and the system which is essential for the optimum design of insulation and determination of protection level in the HVDC system[1,2].

A review of the literature shows that a few of the operating conditions/parameters which have significant influence on the transient voltage distribution have not, been sufficiently, and in certain cases not at all, considered. Some of these are:

a) the influence of conducting modes of the converter valves,
b) effects of terminal apparatus like transformer and reactor,
c) the influence of terminal conditions of the converter both on AC and DC sides,
d) natural frequencies of the valve group and system,
e) incident surge voltages of high rate of rise, and
f) effects of various stray capacitances in the system.

These factors need to be considered as the DC terminal consists of converter valve along with terminal apparatus like converter transformer and smoothing reactor. The different valve groups in the converter will always be in either conducting mode or blocked mode under grounded or isolated terminations of negative pole, secondary neutral and the reactor terminal and hence a knowledge of these terminal conditions is important. The natural frequencies of the converter and that of the system have a significant influence on the rate of rise of voltage at different points in the valve and also on the voltage across different modules in the valve. Further, as the valves are highly sensitive to dv/dt, this knowledge can help in achieving a better operation of the system. Incident surges with high front time of the order of 0.1μs are likely to occur due to terminal flashovers to ground particularly in gas-insulated ubstations. Such surge voltages also significantly affect the transient voltage distribution in the valve. Taking these factors into consideration the analysis of voltage distribution is carried out in an integrated HVDC terminal network consisting of transformer, reactor and HVDC valves for both conducting and blocked modes of different valve groups in the converter.

The integrated network is represented by a mathematical model incorporating a modular structure of the converter. The thyristor is modelled by a high inductance[3] which is better compared to its representation by a conventional switch. The transformer and the reactor are represented by LC ladder networks taking inter and intra capacitive and inductive couplings between sections.

An approach based on frequency domain analysis is adopted in places of the time domain analysis followed by other earlier investigators as it takes into consideration the distributed nature of couplings in different components of the integrated HVDC network. This method helps to evaluate the natural frequencies of the system through the eigenvalue technique and hence to study the transient voltage distribution along the integrated network for different conduction modes and terminal conditions.

Several case studies, based on these important operating conditions/parametric variations, have been considered so as to identify the influence of:

a) negative pole termination
b) reactor termination
c) modes of conduction
d) point of application of surge, and
e) disconnection of terminal apparatus.

on the transient voltage, its rate of rise and voltage across modules and modular units in the converter valve. In all these cases the incident surge is assumed to be a fast-front transient.

It has been thus established, for the first time, that transient voltage study is possible in the integrated network consisting of converter, converter transformer and reactor under various terminal conditions when it is subjected to fast front surges at different points on the system.

3. Conclusions

1. The *surge at positive pole* of the converter bridge is the worst condition experienced, with a maximum voltage of 0.869 pu across the modules adjacent to the point of surge. Hence, these modules need higher insulation level as compared with others thus achieving a more optimal design of the insulation co-ordination of the converter valves.

2. There is an appreciable increase in the node-to-datum voltage when the *negative pole is isolated*, for different surge conditions, and an increase of more than 40% is observed in certain cases.

3. During the *2-valve conduction mode* the rate of rise of voltage along the converter limbs increases to a value as high as 1.147 pu/μs which can cause maloperation of the bridge.

4) The increase in the node-to-datum voltage along the converter when the *reactor terminal is isolated* is not much, whereas it is quite significant along the reactor.

An attempt has been made to optimise the capacitances of the snubber circuit and bushings which play a dominant role in the transient voltage distribution. The concept of providing higher insulation and voltage rating for a few modules in a valve group has been proposed for the first time.

References

1. KRISHNAYYA, P. C. S. Voltage and current stresses on HVDC valves, *Electra*, July 1989, No. 125, 57–87.

2. ARRILLAGA, J. AND EL-BATAL, S. Lightning-surge distribution in HVDC converters, *Proc. IEE*, 1973, **120**, 595–600.

3. RAJAGOPALAN, V. *Computer aided analysis of power electronics systems*, 1987, Marcel-Dekker.

Thesis Abstract (Ph.D.)

Total synthesis of sesquiterpenes containing multiple quaternary carbons

by K. Krishnan

Research supervisor: A. Srikrishna
Department: Organic Chemistry

1. Introduction

The presence of quaternary carbon atoms is frequently encountered in natural products, particularly in terpenoids. Although there are several methods available for the construction of carbon–carbon bond, the presence of two or more quaternary carbons in a contiguous manner in natural products often makes them challenging synthetic targets. Herein we describe the use of Claisen rearrangement and intramolecular diazoketone cyclo-propanation reactions for the regio- and stereoselective construction of vicinal quaternary carbons present in sesquiterpenes.

2. Results and discussion

2.1. *Synthesis of thapsanes*

Recently a series of thapsanes, both hemiacetalic **1-5** and open form **6-7** have been isolated from the Mediterranean umbelliferous plant *Thapsia villosa var minor*[1-4]. A characteristic of this new class of hemiacetalic sesquiterpenes is the presence of unique 3b, 4, 4, 7a-tetramethyldecahydroindeno[1,2-c]furan moiety incorporating three contiguous quaternary carbons posing a significant synthetic challenge. The synthesis of (±)–3a, 4, 4, 7a-tetramethylhydrindan-2-one (**8**), containing three contiguous quaternary carbons as present in thapsanes; first total synthesis of thapsenes **9** and **10**, probable biogenetic precursors of natural thapsanes; and first total synthesis of a natural thapsane **5** are described in the first chapter[5-9]. Thus, *ortho* ester Claisen rearrangement of cyclogeraniol **11**, followed by hydrolysis of the resultant ester **12** furnished the eneacid **13**. Anhydrous copper sulphate-catalyzed intramolecular cyclopropanation reaction of the diazo ketone **14** derived from the acid **13** generated the cyclopropylketone **15**. Regiospecific reductive cleavage of cyclopropylketone **15** furnished the hydrindanone **8**, whereas the diazoketone **16** furnished the hydrindanone **17** *via* the cyclopropyl ketone **18**. Wittig methylenation of the hydrindanone **17** furnished the thaps-7(15)-ene(**9**) which on isomerisation gave thaps-6-ene (**10**). On the other hand, Claisen rearrangement of cyclogeraniol **11** with methoxypropene catalyzed by propionic acid provided the enone **19**. Rhodium acetate-catalyzed intramolecular cyclopropanation of α-diazo-β-ketoester **20** obtained from the enone **19** *via* the β-ketoester **21** furnished the cyclopropylketone **22**. Reductive cleavage of the cyclopropylketone **22** afforded a 1:1 mixture of the hydrindanone **23** and the decalin system **24**. Wittig olefination of the hydrindanone **23** furnished the eneester **25**. Epoxidation of the eneester **25** followed by BF_3OEt_2-catalyzed rearrangement of the epimeric epoxides **26** afforded the hemiacetal **27**. Ionic hydrogenation of the hemiacetal **27** furnished the lactone **28** and finally DIBAH reduction of the lactone **28** furnished the natural hemiacetalic thapsane **5**.

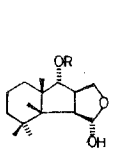

1 R = Ang =

2 R = Sen =

3 R = Coum =

4 R = Fer =

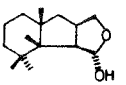

5

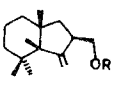

6 R = H

7 R = Fer

8

9

10

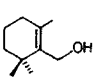

11

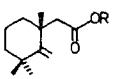

12 R = Et

13 R = H

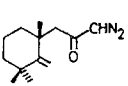

14

15

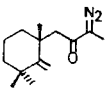

16

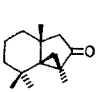

18

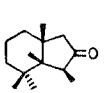

17

19

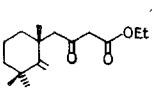

21

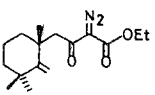

20

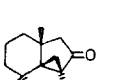

22

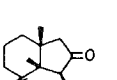

23

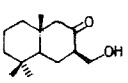

24

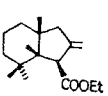

25

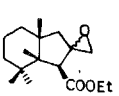

26

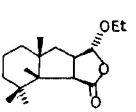

27

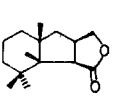

28

CHART I.

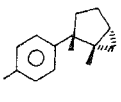

29

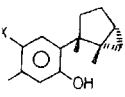

30 X = Br
31 X = H

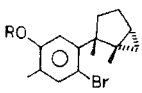

32 R = H
33 R = Ac

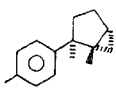

34

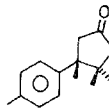

35

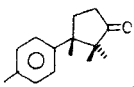

36

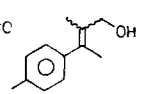

37

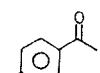

38

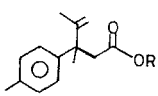

39 R = Et
40 R = H

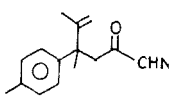

41

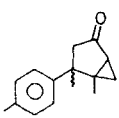

42

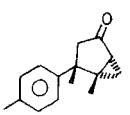

42a

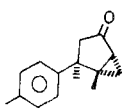

42 b

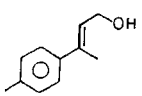

43

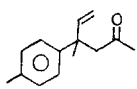

44

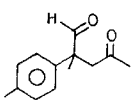

45

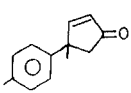

46

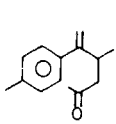

47

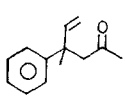

48

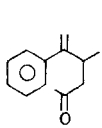

49

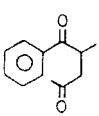

50

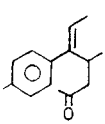

51

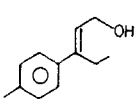

52

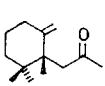

53

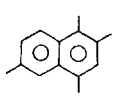

54

CHART 2

2.2. *Synthesis of cylolaurenes and cuparenones*

Recently, Higa and Ichiba have reported the isolation[5] of cyclolaurene (**29**), the parent hydrocarbon of the tricyclic aromatic sesquiterpenes laurinterols[6] **30–31** containing two vicinal quaternary carbons, from sea hare, *Aplysia dactylomela* along with cyclolaurenols **32–33**. The bicyclic sesquiterpenes β-cuparenone (**35**) and α-cuparenone (**36**) were isolated from the ketonic fraction of *Thuja orientalis* and later their presence was detected in various essential oils. The first total synthesis of (±)-cyclolaurene (**29**) and (±)-epicyclolaurene (**34**) and new routes to (±)-β-cuparenone (**35**) and (±)-α-cuparenone (**36**) are described in the second chapter[10-11]. The *ortho* ester Claisen rearrangement of the cinnamyl alcohol **37**, prepared in two steps from *p*-methylacetophenone **38**, followed by hydrolysis of the resultant ester **39** furnished the eneacid **40**. Anhydrous copper sulphate-catalyzed intramolecular cyclopropanation reaction of the diazo ketone **41** obtained from the acid **40** provided a diastereoisomeric mixture of cyclopropyl ketone **42**. Huang–Minlon modified Wolff–Kishner reduction of the cyclopropyl ketones **42a** and **42b** resulted in the formation of (±)-cyclolaurene (**29**) and (±)-epicyclolaurene (**34**). Whereas the regiospecific cyclopropane cleavage of the epimeric mixture of cyclopropyl ketone **42** furnished the (±)-β-cuparenone (**35**). On the other hand, one pot Claisen rearrangement of the cinnamyl alcohol **43** obtained in two steps from *p*-methylacetophenone **38** with methoxypropene and propionic acid provided the γ, δ-unsaturated hexenone **44**. Ozonolysis of the hexenone **44** followed by base-catalyzed intramolecular aldol condensation of the resultant ketoaldehyde **45** with base furnished the cyclopentenone **46**, a known precursor to α-cuparenone (**36**)

2.3. *Rearrangement of γ, δ-unsaturated ketones*

Acid-catalyzed thermal rearrangement of γ, δ-unsaturated ketones to isomeric γ, δ-unsaturated ketones *via* an intramolecular ene reaction of the enol tautomer followed by a retro ene reaction (enolene rearrangement) is described in the third chapter Thermal activation of enone **44**, the Claisen rearrangement product of the cinnamyl alcohol **43** in the presence of a catalytic amount of propionic acid furnished a 2:1 mixture of the rearranged **47** and starting **44** enones. Similarly, thermolysis of the corresponding phenyl compound **48** generated the rearranged enone **49**, which on ozonolysis furnished the known diketone **50** confirming the structures of the rearranged enones. The formation of enone **51** containing an extra methyl group on the styrene double bond starting from the cinnamyl alcohol **52** confirmed the proposed mechanism. Finally, the rearrangement has been extended to the enone **19** by its thermal conversion to the enone **53**. Interestingly, microwave irradiation of the enone **44** on montmorillonite K-10 support using a commercial microwave oven furnished the naphthalene **54** *via* cyclisation and aromatisation of the enone **47**.

References

1. LEMMICH, E., JENSEN, B. AND RASMUSSEN, U. — *Phytochemistry*, 1984, **23**, 809–811.
2. PASCUAL TERESA, J. D., MORAN, J. R. AND GRANDE, M. — *Chem. Lett.*, 1985, 865–868
3. PASCUAL TERESA, J. D , MORAN, J. R., FERNANDEZ, A. AND GRANDE, M — *Phytochemistry*, 1986, **25**, 703–709 & 1171–1174.
4. SMITT, U.W., CORNETT, C., NORUP, E. AND CHRISTENSEN, S. B. — *Phytochemistry*, 1990, **29**, 873–375.
5. ICHIBA, T. AND HIGA, T. — *J. Org. Chem.*, 1985, **51**, 3364–3366.
6. IRIE, T., SUZUKI, M., KUROSAWA, E. AND MASAMUNE, T. — *Tetrahedron*, 1970, **19**, 3271–3277.
7. CHETTY, G. L. AND DEV, S. — *Tetrahedron Lett.*, 1964, 73–77.
8. SRIKRISHNA, A. AND KRISHNAN, K. — *Tetrahedron Lett.*, 1989, **30**, 6577–6580
9. SRIKRISHNA, A. AND KRISHNAN, K. — *J. Chem. Soc., Chem. Commun.*, 1991, 1693–1694.

10. SRIKRISHNA, A. AND KRISHNAN, K. *Tetrahedron*, 1992, **48**, 3429–3434.

11. SRIKRISHNA, A. AND KRISHNAN, K. *Indian J. Chem. B*, 1990, **29**, 679–680.

Thesis Abstract (Ph.D.)

Buckling of laminated anisotropic axisymmetric shell panels/shells with laminated anisotropic stiffeners by Biswajit Tripathy

Research supervisor: K. P. Rao
Department: Aerospace Engineering

1. Introduction

Axisymmetric shell structures made of laminated composites are used extensively in all engineering applications. Buckling is one of the important modes of failure of shells when they are thin, as is the case most often in all aerospace applications[1–4]. In order to meet the stiffness and strength requirements, keeping in mind the minimum weight consideration, these shells are made of stiffened/sandwich construction. Addition of stiffeners may change the buckling load and mode of the structure entirely depending on the size and location of these stiffeners, material properties, loading and boundary conditions Such a construction has to be modelled appropriately to represent the realistic behaviour of the shell. This work presents the work done on the buckling problem of laminated anisotropic axisymmetric shell panels/shells with laminated anisotropic stiffeners (in meridional and hoop directions), using finite element method.

In designing a composite shell with composite stiffeners along meredian and parallel circle directions, the designer has several parameters to contend with, such as geometry of the shell, fiber angles, the stacking sequence, spacing between stiffeners and their locations, etc. Among these, orientation angles and stacking sequence of the plies are found to have significant effect on the buckling load of the structure. This makes it imperative to investigate the ways to optimize the composite layup and exploit its directional property. In this work a way to find the optimum layup scheme of plies in the shell and stiffener layup that will give the maximum buckling load factor for a given geometry, loading and boundary conditions is proposed and several cases are addressed.

2. Present work

Linear bifurcation buckling model is used in the prediction of buckling loads for stiffened composite axisymmetric shell panels/shells. A four-noded, 48-d.o.f. doubly curved quadrilateral laminated anisotropic thin shell finite element with fully compatible two-noded, 16-d.o.f. meridional stiffener element (MSE) and parallel circle stiffener element (PCSE) (Fig. 1) are used. The geometric stiffness matrices are formulated from the nonlinear strain–displacement relationships for the shell and stiffener elements. Eccentricity of the stiffeners is taken into account. Continuity of displacements and their derivatives at the shell–stiffener interface is maintained. The shell and the stiffeners can be of solid or sandwich construction. The sandwich shell can have a sinusoidally corrugated core, hat-type corrugated core or a regular grid core. The stiffener laminate can be parallel or perpendicular to the shell middle plane. Buckling loads for several cases of plain/stiffened shell panels/shells (of positive, zero and negative Gaussian curvatures) subjected to different loading and boundary conditions are computed using the code developed and the results compared with those existing in literature.

In the exercise of optimization of the ply location and orientation (from buckling point of view), the composite shell and the stiffener are assumed to be made of repeated sublaminate construction. This type of construction is used in industry to reduce manufacturing errors and to produce more damage tolerant laminates. In repeated sublaminate construction, the sublaminate consists of smaller number of piles, for example, 2, 4,

6 or 8, and the required thickness of the laminate is obtained by repeating the sublaminate many times The present work deals with the determination of the optimum layup scheme in the sublaminate of plain/stiffened composite axisymmetric shell so as to achieve the maximum buckling load for given geometry, loading and boundary conditions The plies in the sublaminate can be oriented at any of the chosen four angles θ_1, θ_2, θ_3, and θ_4. The 2- and 4-ply sublaminates are assumed to be bi-directional, 6- and 8-ply sublaminates are assumed to be tri- and quadri-directional, respectively. Thus several possible layup

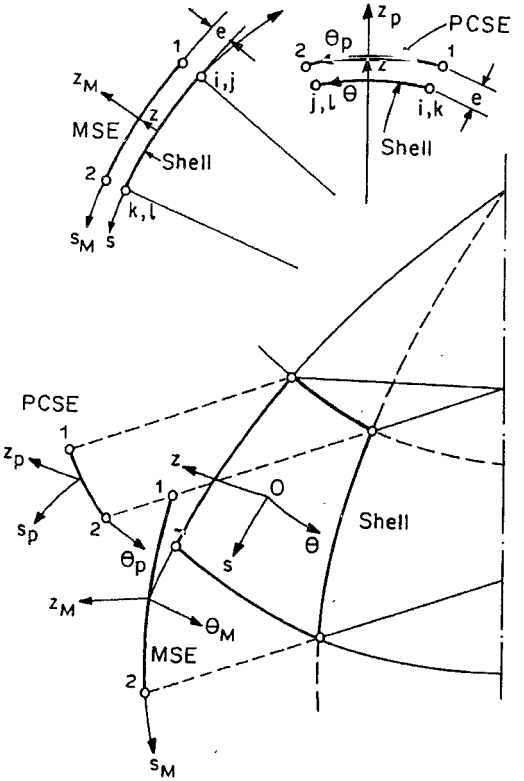

FIG. 1. Doubly curved quadrilateral shell finite element with compatible meridional (MSE) and parallel circle (PCSE) finite elements.

schemes in the sublaminate are found and stored in the data bank of the computer code Buckling loads are computed for all of these layup schemes and rank ordered. The layup scheme is optimum corresponding to which the buckling load is maximum.

3. Conclusions

Linear bifurcation buckling of fiber reinforced composite stiffened shells is solved using finite element method. A four-noded, 48-d.o.f. doubly curved quadrilateral laminated anisotropic shell finite element with fully compatible two-noded, 16-d o f. meridional and parallel circle stiffeners are used. Correctness of the code is checked by solving several examples and comparing the results with those available in literature.

Optimum layup schemes for several cases of plain/stiffened shells/shell panels subjected to different loading and boundary conditions are obtained. It is observed that location as well as orientation of the piles play a significant role in deciding the buckling load. It is also observed that for general fiber reinforced plastic shells (plain/stiffened) of given geometry and subjected to general loading and boundary conditions, it is extremely difficult to predict the layup scheme a priori, that will give the highest buckling load. In such cases, it is believed, a rank-ordered table which the code developed generates, will be of significant practical use to the designer.

References

1. BUSHNELL, D. *Computerized buckling analysis of shells,* AFWAL-TR-81-3049, Wright Patterson AFB, OH, 1981.
2. LEISSA, A. W. *Buckling of laminated composite plates and shell panels,* AFWAL-TR-85-3069, Air Force Wright Aeronautical Laboratories, Wright-Patterson AFB, OH, 1985.
3. VENKATESH, A. *Finite element analysis of laminated anisotropic shells with laminated anisotropic stiffeners,* Ph.D. Thesis, Indian Institute of Science, Bangalore, India, 1982.
4. TSAI, S. W. *Composite design,* 4th edn., Sec. 9.8, 1988, Think Composites.

Thesis Abstract (Ph.D.)

Architecture, performance and applications of a hierarchical network of hypercubes

by J. Mohan Kumar

Research supervisor: L. M. Patnaik
Department: Computer Science and Automation

1. Introduction

In recent years, considerable progress made in the design of integrated circuit technology has resulted in the emergence of highly powerful processors. Several new parallel architectures have been proposed. But to this day the problem of interconnecting processors to achieve high computational bandwidth has not been fully solved. Increased parallelism means more communication among processors and hence a corresponding increase in communication overheads. Internode distance, message traffic density and fault-tolerance are dependent on the diameter and degree of connectivity. The product (diameter* degree[1] of connectivity) is a good criterion to measure the cost and performance of a multiprocessor system[1]. An interconnection network with a large diameter has a very low message passing bandwidth and a network with a high degree of connectivity is very expensive.

The choice of a suitable interprocessor communication scheme is a very important criterion in the design of message passing, distributed memory multiprocessor systems. Several multiprocessor topologies have been proposed by researchers to meet the demands of an efficient multiprocessor system. The binary hypercube has a regular structure and its topology is well suited for the implementation of a large class of parallel algorithms[2]. However, the binary hypercube structure has several shortcomings. Several modifications of the binary hypercube topology have been suggested to overcome some of the shortcomings of the hypercube. The cube-connected cycles, the hypertree, the hypernet, the folded hypercube, and the twisted hypercube are some of the hypercube-related architectures[3]. In this work, we present a new topology, *viz.*, the hierarchical network of hypercubes, also known as the extended hypercube (EH), whose diameter is lower than those of topologies such as binary hypercube, mesh, hypernet, and hyper tree with identical number of nodes[3]. The degree of connectivity of the processor element of the hierarchical network of hypercubes is a constant value unlike that of topologies such as hypercube, and folded hypercube. For the same number of processor elements, the cost factor of the proposed network is lower than those of hypercube, folded hypercube, ring, mesh, binary tree and many others. The utilization factor of the network is higher than those of all other topologies except those which have a separate communication processor at every node and the fully connected network. The network has a predefined constant basic building block. The hierarchical network of hypercubes is found to be suitable for the execution of a large class of problems such as ASCEND/DESCEND, multinode broadcast, and total exchange. The ASCEND/DESCEND class of algorithms find application in several problems such as bitonic sort, FFT analysis, and convolution. The multinode broadcast and total exchange problems are encountered in the simulation of artificial neural networks. In this work we address the problem of simulating artificial neural networks on the hierarchical network of hypercubes.

Artificial neural networks (ANNs) are being used to solve a variety of problems in pattern recognition, robotic control, VLSI CAD, etc. In most of these applications a speedy response from the ANN is imperative. However, the ANNs comprise a large number of artificial neurons and a massive interconnection network among the neurons. Hence, simulation of ANNs involves execution of compute-intensive problems and communication tasks, *viz.*, multinode broadcast and total exchange[4]. Our studies reveal that the hierarchical network of hypercubes is well suited for the implementation of artificial neural networks. We discuss implementation of ANNs on a transputer-based EH for applications in robotic control.

2. Hierarchical network of hypercubes

The EH architecture is suited for hierarchical expansion of multiprocessor systems. The basic module of the EH consists of a k-cube and an additional node for handling communication–the network controller (NC). There are a total $[2^{**}(k/2 + 1)]$ links in the basic module, consisting of the $[(2^{**}k)/2]$ links of the hypercube and 2^k links between the individual processor elements and the NC, as indicated in Fig. 1. An EH consisting of a k-cube and one NC will be referred to as the basic module or EH(k, 1). The EH(k, 1) has two levels of hierarchy: a k-cube at the zeroth level and an NC at the first level. The hypercube consisting of the PEs is referred to as the HC(k, 0). An EH(k, 2) has 2^k k-cubes of processor elements (PEs) at the zeroth level, a k-cube of NCs at the first level and one NC at the second level. In general, an EH(k, *l*) (*l* is the degree of the EH), consists of a k-cube of 2^k NCs/PEs at the (*l*-1)st level and one NC at the *l*th level. The NCs/PEs at the (*l*-1)st level of hierarchy form a k-cube. We refer to this cube as HC(k, *l*-1). The NCs at the (*l*-2)nd level of hierarchy from 2^k distinct k-cubes which are called HC(k, *l*-2). The HC(k,0)s are all computation HCs and the HC(k, *l*)s (for $l > 0$) are all communication HCs. The basic module of the EH denoted by EH(k,1) is a constant pre-defined building block and the node configuration remains the same regardless of the dimension of the EH. The EH architecture can easily be extended by interconnecting appropriate number of basic modules. For example, we can interconnect eight EH(3, 1)s (basic modules) to get a 64-node EH-an EH(3, 2) of Fig. 2. The topology formed by the 3-cube of NCs at the first level, and the controller at the second level, is identical to that of the basic module. Thus we have a hierarchical structure consisting of 64 PEs at the zeroth level (lowest level), eight NCs at the first level, and one NC at the second level. The EH has two types of links, *viz.*, hypercube links which form the k-cubes and the EH links which connect the nodes at the jth level to the nodes at (j + 1)st level. Further, the path between any two PEs of the EH via one or more NCs is called an extended link.

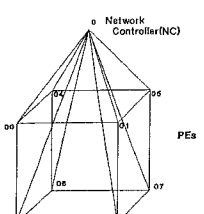

FIG. 1 Basic module of the extended hypercube, EH (3,1)

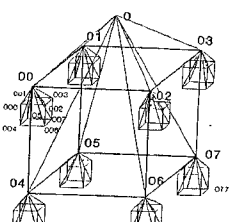

FIG 2. EH (3,2).

The nodes of the EH are addressed as described below. The address of an arbitrary node at the zeroth level is written as $D_l D_{l-1} ... D_i ... D_0$, where D_i $(0 \le i \le l)$ is a k-bit mod 2^k number, *e.g.*, in an EH(3, *l*), D_i is a 3-bit mod 8 number. In an EH(k, *l*) a node at the zeroth level has an $(l + 1)$-digit address, a node at the first level has an *l*-digit address..., the solitary node at the *l*th (topmost) level has a single digit address. The NC at the top-most level retransmits messages to/from the host system from/to the PEs *via* the hierarchical network of NCs. In an EH(k,1), message passing between neighbouring nodes of the hypercube is *via* the direct communication links among them whereas communication between non-neighbouring nodes of the hypercube is *via* the NC. Message passing operation in local communication (within a k-cube) involves 1) the source PE, 2) up to (k-1) PEs within the k-cube, and 3) the destination PE, whereas message passing operation in global communication involves 1) the source PE, 2) up to 2(*l*-1) NCs, and 3) the destination PE.

3. Simulation of artificial neural networks

ANNs are being used extensively for solving a variety of problems related to pattern recognition and analysis. Various ANNs have been proposed in recent years to mimic the human brain in solving problems which involve human-like intelligence. The simulation of ANNs comprising a large number of neurons is a compute-intensive problem. Further, the massive interconnection among neurons demands a communication-efficient architecture.

Each artificial neuron or neural cell is a simple computing element. ANN models which comprise a large number of artificial neurons are specified by the net topology, node characteristics and learning rules. The ANN models are simulated on computing systems to assess the learning algorithms for their suitability in various applications. Overall, the architectural support currently available for simulating ANNs is found to be inadequate since with the current technology it has been possible to simulate up to $O(10^6)$–$O(10^7)$ artificial neurons on parallel architectures whereas the human brain consists of $O(10^{10})$–$O(10^{11})$ neurons The ANNs are characterized by completely distributed memory, asynchronous processing and inherent fault-tolerant capabilities. Consequently ANNs are amenable to mapping on multiprocessor architectures having a large number of processing elements and supported by an efficient communication scheme. Multiprocessor systems offer a relatively inexpensive means for simulating a large number of neurons.

Typically, simulation of ANNs on message passing architectures comprises execution of matrix-vector multiplications and message passing among the neurons mapped on to the processor elements of the system. The communication tasks consist of multinode broadcast and total exchange. Our studies reveal the necessity of communication-efficient architectures to handle distributed message passing among the PEs of a multiprocessor system. In ANN simulation, the overall efficiency of a multiprocessor system is greatly affected by the

amount of communication tasks each PE is required to execute. Our studies reveal that ANN paradigms such as backpropagation network and CMAC can be implemented on a transputer-based EH for robotic applications.

4. Results and discussions

The hierarchical network of hypercubes (or EH) is an expansive, and recursive structure with a predefined basic building block. For identical number of processor elements, the diameter of the EH is lower than those of the binary hypercube, the mesh, the ring, the hypernet, and the cube-connected cycles. The degree of connectivity of the EH is lower that of the hypercube, and the folded hypercube, and the cost factor of the EH is lower than those of most other multiprocessor topologies, viz., ring, mesh, hypercube, hypertree, hypernet, cube connected cycles etc. as shown in Fig. 3. There are k + 1 parallel paths for message passing within every k-cube of the EH. The use of network controller nodes for each k-cube ensures efficient and fault-tolerant communication of messages. The ASCEND/DESCEND class of algorithms for N data elements can be executed in O(log N) parallel steps on an EH with N PEs. The utilization factor of the EH is higher than those of all other multiprocessor topologies except those which possess one communication processor per node and the fully connected network as shown in Fig. 4. The use of NCs in the EH facilitates efficient implementation of error detection algorithms which run concurrently with the application programs. We find that the per cent error coverage is very high and yet the per cent error detection overhead while executing algorithms related to matrix multiplication and implementation of ANNs is relatively small. In the case of link faults, the additional links among PEs and NCs are effectively used to achieve fault-tolerant message routing. The fault-tolerant extended hypercube, a simple modification of the original EH, exhibits fault-tolerant characteristics comparable to those of the folded hypercube, but superior to those of the EH and binary hypercube topologies.

Our studies reveal that the extended hypercube which has dedicated processor for handling communication tasks performs better than other topologies such as ring, mesh, binary tree, and hyper-cube. In our study we have used T 800 transputers to experimentally demonstrate the advantages of the EH topology for simulating ANNs. The results of simulation studies are indicated in Table I. From our studies it is found that the hierarchical network of hypercubes can be used for meeting the real-time requirements of robotic processing. Our experimental studies show that the ANNs implemented on the transputer-based EH can produce responses (execute one iteration of the ANN algorithm) within hun-dred microseconds.

Problems with dense local communication, and sparse global communication among the subtasks of the problem can be executed very efficiently on the EH since the localized message traffic density of the EH is lower than those of most other topologies except the fully connected network. Research in the direction of implementing problems such as clustering algorithms, FFT analysis, genetic algorithms on the EH is most likely to produce good results. The structure of the EH is most suitable for building larger systems by putting together smaller ones. Hence, the EH is a very good candidate for constructing commercial multiprocessor systems based on any conventional microprocessor or transputer. Moreover since the degree of connectivity of each processor element is very low(k + 1), it is less expensive to build an EH-based distributed memory message passing multiprocessor system.

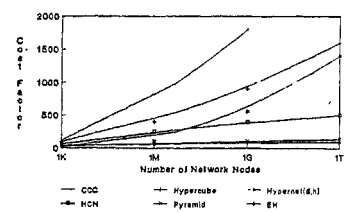

FIG. 3. Comparison of cost.

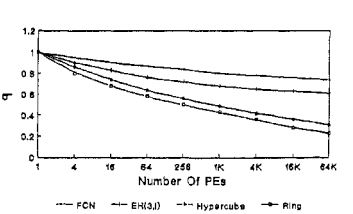

FIG. 4. Utilization factor for different topologies.

Table I. Execution time for one iteration of backpropagation algorithm

Size of network (Number of cells)	Execution time (s) for one iteration			
	Ring 64-node	Hypercube 6-cube	Hypernet (4,2)	EH (3,2)
256 × 1024 × 256	0.0686	0.0641	0.6520	0.0549
1024 × 4096 × 256	1.1210	1.0560	1.1004	0.8023
1024 × 4096 × 1024	4.6410	4.2134	4.3514	3.0126

References

1. BHYAN, L. N. AND AGRAWAL, D P. Generalized hypercube and hyperbus structures for a computer network, *IEEE Trans.*, 1984, **C-33**, 323–333.
2. SAAD, Y. AND SCHULTZ, M. H. *Topological properties of hypercube*, TR RR-462, Yale University, 1988.
3. MOHAN KUMAR, J. AND PATNAIK, L. M. Extended hypercube: A hierarchical network of hypercubes, *IEEE Trans.*, 1992, **PDS-3**, 45–58.
4. PATNAIK, L. M. AND MOHAN KUMAR, J. Distributed memory systems for simulating artificial neural net works, *Computers Electl. Engng*, 1993, **19**, 431–443.

Thesis Abstract (Ph.D.)

Analysis of electro-optic waveguide modulators using finite difference formulations

by M. V. Sathyanarayana

Research supervisor: A. Selvarajan
Department: Electrical Communication Engineering

1. Introduction

Electro-optic modulators are essential components in most of the optical communication and optical instrumentation systems. Electro-optic phase modulation is the most basic type of optical modulation. The field of electro-optic modulator is now several decades old. Such modulators are normally fabricated by realizing waveguides on $LiNbO_3$ substrates. The modulating voltage is applied through a set of coplanar electrodes printed either adjacent to or with one of the electrodes directly on top of the waveguide.

The present work aims at analyzing the performance characteristics of electro-optic modulators using finite difference formulations. Finite difference techniques are becoming popular now-a-days because of their simplicity and the ease with which they can be adapted for simulation purposes.

Analysis of electro-optic waveguide modulators is done in three steps.

1) Evaluation and analysis of the induced electric field as a result of the applied modulating electrical signal.

2) Optical waveguide analysis.

3) Evaluation of the device performance which makes use of the results obtained in the first two steps.

In the present work finite difference method formulations for the electric field analysis, optical waveguide analysis and performance analysis of electro optic waveguide modulators have been derived. These formula-

tions have been tested on standard integrated optical structures, compared with the results obtained through other standard methods and validated.

2. Index perturbation method

In this an alternative method for waveguide analysis in the presence of electro-optic effect is presented. In Ti:$LiNbO_3$ waveguides the index profile can be approximated by smoothly varying functions of depth and width. The nature of the index profile can be assumed to be Gaussian–Gaussian, Gaussian–erfc, etc., for analysis purposes. When the index profile is further perturbed by the electro-optic effect, the profile becomes somewhat arbitrary.

Conventionally the waveguides in the presence of electro-optic effect are analysed using an overlap integral which accounts for normally incomplete overlap between the applied electric field and the propagating optical field. The induced phase shift is then calculated as a function of the overlap integral along with the relevant index and the electro-optic coefficient

In the method suggested the waveguide is treated as having an arbitrary index profile in the presence of electro-optic effect the graded index profile of the waveguide is analysed to obtain the propagation constant of the guide β_1. In the second step the new index profile is determined in the presence of electro-optic effect. Next the new propagation constant β_2 is determined. Finally the induced phase shift is calculated as $\Delta\phi = (\beta_2 - \beta_1) L$ where L is the interaction length.

This method appears to be more logical than the conventional one. The results obtained in this method compares favourably with the experimental results obtained elsewhere[1].

3. Electric field analysis

The electric field analysis is an important step in the performance analysis of electro-optic waveguide modulators. In this work a survey of the several methods proposed so far is carried out. A finite difference algorithm for the purpose is derived.

For simulation purposes a device model similar to a shielded coplanar micro strip line on a layered anisotropic dielectric substrate is assumed. The waveguide is planar having a buffer layer above the guiding region. The electrodes are assumed to be negligibly thin and symmetric with respect to the inter-electrode gap.

The finite difference algorithm derived is as follows[2].

$$\left(\frac{\epsilon_{x1}+\epsilon_{x2}}{2}\right)\left(\frac{aV_B+bV_A}{(a+b)ab}\right)+\left(\frac{q\,\epsilon_{y1}\,V_C+p\,\epsilon_{y2}\,V_D}{(p+q)pq}\right)-\left(\frac{\epsilon_{x1}+\epsilon_{x2}}{ab}+\frac{\epsilon_{y1}+\epsilon_{y2}}{pq}\right)\frac{V_O}{2}=0$$

where O is the point of interest and A, B, C and D are the surrounding sample points. The potential at the point O is determined in terms of the potentials of the surrounding points. Initially, suitable values are assumed for the potential at various points of interest. Knowing the boundary and initial potentials one can arrive at the potential at any point of interest through iterations. The iterations stop once the potential values between successive iterations converge.

The potential values and the various field components were evaluated using the algorithm. The results compare favourably with the results obtained using the point matching method[2].

The merits of the method are that it is simple and straight forward. Another unique advantage of the method is that the same formulation can be used for any number of additional layers unlike other methods like the point matching method which require reformulation for every additional layer.

4. Curved optical waveguide analysis

Curved optical waveguides from integral parts of optical integrated circuits. Curvatures and bends in waveguides play an important role in determining the density of optical integrated circuits. In this work an

algorithm for determining the propagation characteristics in curved optical waveguides in derived. No algorithm which can describe propagation in curved waveguide which connects two straight but perpendicular waveguides has been reported so far. The proposed algorithm is based on an implicit finite difference scheme The algorithm is derived starting from the scalar Helmholtz equation. Using the implicit scheme to represent the first and second partial derivatives the algorithm derived is as follows.

$$a_1(r)E_{r+\Delta r}^{\theta+\Delta\theta} + a_2(r)E_{r-\Delta r}^{\theta+\Delta\theta} + a_3^+(r)E_r^{\theta+\Delta\theta} = -a_1(r)E_{r+\Delta r}^{\theta} - a_2(r)E_{r-\Delta r}^{\theta} - a_3^-(r)E_{r+\Delta r}^{\theta+\Delta\theta}$$

where r and θ describe cylindrical coordinates.

$$a_1(r) = \frac{1}{2(\Delta r)^2} + \frac{1}{4r\Delta r}$$

$$a_2(r) = \frac{1}{2(\Delta r)^2} - \frac{1}{4r\Delta r}$$

$$a_3^+(r) = \mp\frac{1}{(\Delta r)^2} - \frac{2jk_0n_0R}{r^2\Delta\theta} \pm \frac{k_0^2}{2}\left(n^2 - n_0^2\frac{R^2}{r^2}\right)$$

Knowing the field values along r axis in a θ = a constant plane, one can determine the field values along r in a $\theta + \Delta\theta$ = a constant plane. One will have to solve a set of linear simultaneous equations. Crout reduction method can be made use of with advantage because one encounters tridiagonal matrices here. For one propagation step the complete process requires ($5n$-4) operations leading to a computationally very efficient algorithm. This compares very well with FFT–BPM which requires $2n\log_2 n$ operations for each step. For a comparison the method proposed required 636 operations and the FFT–BPM requires 1792 operations.

The algorithm was tested on waveguide models with radii of curvature of 10, 20, 25 mm etc., which one encounters in integrated optics. The mesh width along r direction was assumed as 0.125 μm, computation window as 20 μm, mesh width along θ direction as 0.001 radians, number of sample points along r as 160. The input profile was assumed as Gaussian with more than 80% of the power confined to the waveguide.

The results obtained were compared with an analytical method which is however applicable only for waveguide of large radius of curvature. The results agree to a large extent.

Another beam propagation method based on the Lebedev Kontorovich transform has also been derived in this work.

5. Inclined and curved waveguide modulators

A feasibility study of curved and inclined waveguide modulators has been carried out as part of the work. The study makes use the finite difference algorithms derived earlier for the electric field analysis and optical waveguide analysis. Traditionally modulators are realized with waveguide parallel to one of the principal axes of $LiNbO_3$ substrate. In this study modulators realized using waveguides inclined at an angle to one of the principal axes and curved waveguides simulated and the relative performances of such devices with respect to conventional type of modulators were evaluated. Various possible configurations such as combinations of straight and inclined waveguide were considered. The study shows that the waveguides need not be parallel to any of the principal axes and that the performance of such modulators is normally only marginally inferior to that with conventional modulators and in some cases even exceeds their performance. The advantage to be gained by making use of curved and inclined portions of the waveguides for device fabrication is in terms of increase chip density.

References

1. Tench, R. E., Delavaux, J. M., Tzeng, L. D., Smith, R. W., Buhl, L. L. and Alferness, R. C. Performance evaluation of waveguide phase modulators at 1.3 and 1.5 μm, *IEEE J.*, 1987, **LT-5**, 492–500.

2. SATHYANARAYANA M. V., SRINIVAS, T. AND SELVARAJAN, A. Electrostatic field analysis of electrooptic devices, *J. Electromagnetic Waves Applic.* (VSP), 1992, **6**, 143–155.

Thesis Abstract (M.Sc. (Engng))

Studies on an electrochromic switching device based on Prussian blue films and related instrumentation by V. Vinni

Research supervisor: L. Kameswara Rao
Department: Instrumentation & Services Unit

1. Introduction

The electrochromic materials colour under simultaneous insertion of withdrawal of ions and electrons under the influence of electric field. These materials find applications in high-contrast passive displays, smart windows, rear view mirrors in automobiles, batteries and corrosion inhibitors. Typical electrochromic devices utilize multilayer structure comprising an electrochromic thin film and an ionic conductor between a pair of transparent conducting electrodes(TCEs). Lack of versatile all solid state design has been hampering the practical utility of these devices.

Prussian Blue (PB) is an ion insertion-type electrochromic material and known to exhibit electrochromism for many years. It exhibits reversible colour changes between dark blue and total transparency when potassium ions and electrons are simultaneously injected into and ejected out of the PB lattice. Until recently the technique of preparing it in thin film form is not known Currently this material is receiving attention for its potential use in smart window and display applications[1,2]. The present work describes the details of the investigations carried out on the design and development of an electrochromic switching device based on PB films using an all-solid state design. A novel gel-type solid electrolyte has been proposed and examined for its utility as an ionic conductor in the electrochromic switching device. A novel methodology is proposed and implemented to effect laser-assisted colour switching *via* electrochromism for optical memory and spatial light modulator applications.

2. Experimental details and results

The subsystems of the device, namely, the TCE, PB film and the ionic conductor are prepared using the hardware and the instrumentation developed indigenously. The TCEs are prepared by spray pyrolysis technique. The electrochromic PB films are prepared by electrochemical deposition technique. The pellets of conditioned agar agar are prepared by a suitable procedure.

Tin oxide films of thickness 0.72 μm are used as TCEs for the proposed device. The films posses an electrical resistivity of 2.6×10^{-3} ohm m and an average transmittance of 82% in the visible spectrum. The films are prepared by spraying intermittently a chemical mixture of 2 g of $SnCl_45H_2O$ dissolved in 10 ml of isopropyl alcohol[3] on to hot microscopic glass substrates. The substrates are maintained at an average temperature of 400°C during the deposition. A spray gun and a microprocessor-based spray controller developed have been designed and fabricated for the preparation of the above films. The spray controller maintains the substrate temperature variation during deposition within ± 5°C. The techniques such as Vander pauw, spectrophotometry, x-ray photoelectron spectroscopy, x-ray diffractometry and scanning electron microscopy are used to study the electrical, optical, compositional, structural and morphological properties of the films. The films are found to be chemically homogenous, polycrystalline and feature fine-grained morphology.

PB films of thickness 0.81 μm are used in the device. The films are deposited on TCEs by electrochemical deposition technique from an electrolyte containing 20 mM$FeCl_36H_2O$ dissolved in 20mM $K_3Fe(CN)_6$[4]. A compact electrochemical cell and a microprocessor-based electronic control system are designed and fabricated. The control system is designed so as to establish potentiostatic and galvanostatic conditions in the electrochemical cell at various stages of PB film preparation. The deposition potential range for obtaining device quality PB films is estimated by a technique called cyclic voltammetry and is found to be between

0.725–0.69 V *vs* SCE. The PB films are prepared by maintaining a constant current density of 70 $\mu A/cm^2$ in the cell for 5 min. The as prepared films are found to undergo decomposition after a few cycles of reversible switching and thus are not suited for device applications. The as deposited films however found to exhibit reliable and reproducible switching when subjected to a post-deposition conditioning procedure called 'potentiodynamic cycling'. The optical, compositional, structural and morphological properties of the PB films are studied using analytical techniques such as spectrophotometry, X-ray photoelectron spectroscopy, X-ray diffractometry and scanning electron microscopy. The films are found to have an optical density of 0.52, possess chemically homogenous phase, polycrystalline with grain size of 20 Å.

The agar agar powder is conditioned to contain potassium ions as follows. 3 g of agar agar and 40 g of KNO_3 are dissolved in 100 ml boiling water. The solution when cooled down settles in gel form The gel is dried and ground manually to fine powder. 2 g of the above power is pressed to a pellet of diameter 1.25 inch and thickness 1.5 mm. The pellets are suitably moisturized before integrating into the device.

The final device is arranged in the following order: PB-coated TCE + moisturized ionic conductor pellet + TCE. The assembly is held together by a pair of holders. Figure 1 shows the cross section of the device assembly. When a 5 V dc is applied across the device with the PB-coated TCE is given a negative potential, the device is found to switch from dark blue to total transparency in a period of 950 ms. It switches back to dark blue upon the reversal of the field, in 500 ms. The device remains in the transparent switched state without the aid of the sustaining excitation for 36 min. This corresponds to the short-term storage of the device The contrast ratio of the device is estimated as 5:1. The reversible switching cycles of the device are found to be 2500 cycles. Figure 2(a, b) show the device in 'OFF' and 'ON' states, respectively.

Earlier attempts to make electrochromic devices based on PB films using polymer electrolyte are reported to exhibit switching speed 1 to 10 seconds and life time of less than 100 cycles[5,6]. The ionic conductor utilized in the present device aids a long life time with relatively faster switching speed, facilitates easy incorporation of moisture and obviates the additional scattering white back backboard.

The utility of the above device structure could be extended to newer applications such as optical storage and spatial modulators if an additional control is incorporated for the electrochromic switching. In the pres

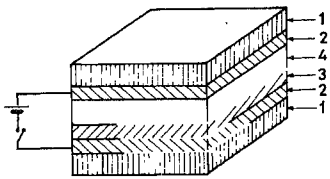

FIG. 1 Cross-section of the device. 1. Glass substrates. 2. Transparent conducting films. 3. Electrochromic Prussian blue film, and 4. Ionic conductor.

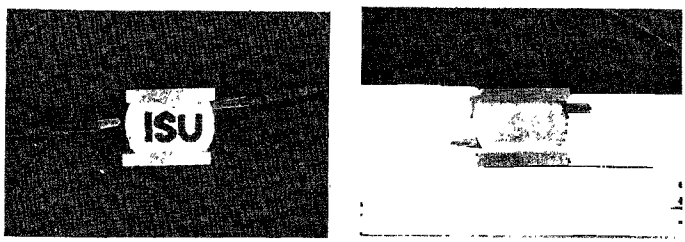

FIG. 2. Photographs of device. (a) OFF state, (b) ON state.

ent thesis a novel methodology is proposed to control the electrochromic switching in the above device by laser irradiation. The PB films require simultaneous insertion of ions and electrons into its lattice for colour switching. The device fails to switch its colour if either the ions or the electrons blocked. In thepresent study it is proposed to block the ions by interposing a thin film of suitable material between the PB film and the ionic conductor. The resistance of the film to ionic flow is then controlled by exposure to laser beam With the electric field on, if a laser beam brings in faster charge transfer either locally or over the entire device, then the laser-assisted colour switching is effectively brought in.

The proposed methodology is examined using a low glass transition temperature (75°C) polymer film of poly vinyl alcohol It is found that when the polymer film is incorporated between the PB film and the ionic conductor, the switching speed from blue to transparency is between 2 and 3 seconds when a 5V dc is applied across the device. When an Ar^+ ion laser beam (514 nm) is focussed onto the PB-coated TCE, the colour switching takes place in the localized laser-irradiated region within 1 second. The above laser-assisted colour switching is observed at the laser power levels from 4 to 7 KWatts/cm^2. When the field is reversed the transparent localized region switches back to blue colour. The storage time is found to be about 30 minutes.

3. Conclusions

1. An electrochromic device of an all solid state design based on PB films using a novel gel electrolyte has been designed and developed The device exhibits relatively faster switching speed and longer lifetime than the currently known devices based on PB films.

2 A novel methodology has been proposed to effect laser assisted colour switching in the electrochromic device. The implemented process gives promises for erase/rewrite type optical storage applications.

3. The requisite hardware and the instrumentation have been designed and fabricated to carry out the above investigations.

References

1. Habib M. A., Maheswari S. P. and Carpenter M. K. — *J. Appl. Electrochem.*, 1991 **21**, 203–207
2. Carpenter M. K., and Connel R. S. — *J. Electrochem. Soc.*, 1990, **137**, 2464–2467.
3. Vasu V., and Subrahmanyam A. — *Thin Solid Films*, 1990, **189**, 217–225
4. Itaya K., Akahoshi H. and Toshima S. — *J. Electrochem. Soc* , 1982, **129**, 1498–1500.
5. Honda K., and Kuwana A. — *J. Electrochem. Soc.*, 1984, **133**, 853–854.
6. Tada H., Bito Y., Fujino K. and Kawahara H., — *Sol. Energy Mater.*, 1981, **16**, 509–516.

Thesis Abstract (Ph.D.)

Studies in fulvene cycloadditions and in optical resolutions by M. Ravindranath

Research supervisor: S. Chandrasekhar
Department: Organic Chemistry

1. Introduction

This thesis is in two parts, the first being on the fulvene cycloadditions and the second on the optical resolutions. Both these studies were motivated by fundamental curiosity.

The fulvene cycloadditions were studied with the hope of discovering new examples of the rare, but theoretically allowed, ($6\pi + 4\pi$) cycloaddition, the few examples already known indeed involving fulvenes as the 6π partners, mostly in dipolar cycloaddition reactions[1]. The 1,3-dipolar cycloaddition of 6,6-diphenylfulvene with a range of C-aryl-N-phenylnitrones is thus reported herein, with emphasis on an analysis of the effect of C-aryl substitutions on regioselectivity.

The optical resolution studies were designed to discover new examples of the spontaneous generation of optical activity, *i.e.*, the obtention of chirality without the intervention of external chirality in systems of potential synthetic interest. Examples of such, necessarily crystallization, processes are not only few and far between, but also involve molecules of apparently little synthetic value[2]. In this study, spontaneous generation of chirality was sought in 1-(4-methoxyphenyl)-2-phenyl-1-propanone, its resolution being also attempted by conventional cyrstallization techniques by seeding with crystals of chirally enriched material. (A novel crystallization technique which improves signi-ficantly the historic Pasteur technique for the manual sorting of conglomerates was designed to obtain the seeds). Finally, useful synthetic transformations of the above propanone are reported.

2. Results and discussion

(Part I). The reaction between 6,6-diphenylfulvene and C,N-diphenylnitrone was studied first (Scheme 1): a single, crystalline, product (**1**) was obtained in 85% yield, structure assignment being based on nuclear Overhauser effect, NMR studies, and X-ray diffraction determination of the crystal structure[3]. It is argued that both concerted and stepwise pathways are possible, the latter on the basis of the stability of the intermediate diradical.

The reaction between 6,6-diphenylfulvene and various C-aryl-N-phenylnitrones was then studied (Scheme 2). The reaction appears to be sensitive to steric effects, but not much to electronic effects, as seen by the nature of the products; the regio- and stereoelectivity shown in Scheme 2 were unchanged when the C-

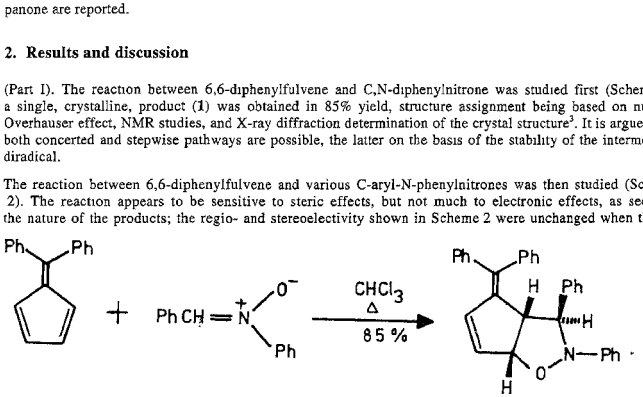

1

SCHEME 1.

aryl substituent were *para* and *meta*, but regio- and stereoisomers were obtained when they were *ortho*. The isomers could be separated chromatographically from each other, and their structures assigned on the basis of NMR. A bis-adduct was also obtained in low yield for the *o*-methoxy case; both the cycloaddition steps occur with the opposite regioselectivity to that shown in Scheme 2, the ring junctions being *syn-anti-syn*; the stereochemistry at the aryl bearing carbon is such that there is no C_2 axis of symmetry in the molecule. Many of these cycloadditions were found to be much faster in the neat melt than in solution.

(Part II). Spontaneous generation of optical activity was observed when propanone (**2**) was crystallized in the presence of 1,8-diazabicyclo[5,4,0]-undec-7-ene (DBU) (Scheme 3)[4]. Ketone (**2**) was chosen for

two reasons: firstly, it was known[2] to exist as a conglomerate, *i.e.*, a mechanical mixture of enantiomeric crystals (as opposed to a racemate in which the enantiomers share the same lattice), and, secondly, the mutual interconversion of the enantiomers is possible in the presence of a strong base (hence DBU), *via* the enolate anion. Crystalline (2) with enantiomeric excess (e.e.) values as high as 100% could thus be obtained, in variable yields. The term, 'preferential spontaneous resolution' has been proposed for pheno-mena such as the above, which are alternatively known as second-order asymmetric transformation of enantiomers[2].

A novel crystallization technique which facilitates Pasteur's mechanical–manual sorting resolution method was designed: the conglomerate is crystallized in a network of cells or compartments, thereby preventing the formation of extended crystals; the crystals within the cells are of very high optical purity, and can be used as seeds for further resolution of the racemic mixture on larger scales. Many grams of (2) were thus obtained in optical purities of about 90%.

Synthetic studies on ketone (2), in order to take advantage of the above successes in optical resolution, were carried out, transformation to bicyclic tetralone (3) having been accomplished (Scheme 4). When (2) of 83% e.e. was used, optically active (3) (but of unknown e.e.) was obtained. Plausible synthetic schemes for conversion of (2) to biologically active compounds possessing similar structural and functional features, *e.g.*, estrone, are discussed.

Diastereoselectivity in the hydroboration–oxidation of styrene (4), first steps in the above transformations (Scheme 4), were studied in some detail using various hydroborating agents (Scheme 5). Explanations for the observed results are proposed.

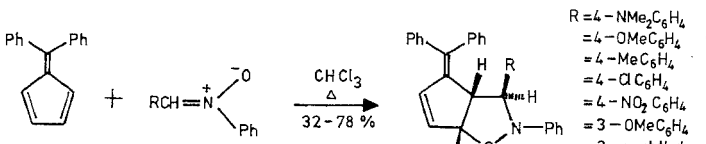

SCHEME 2.

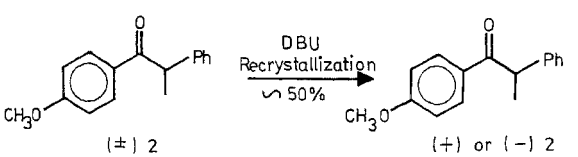

SCHEME 3.

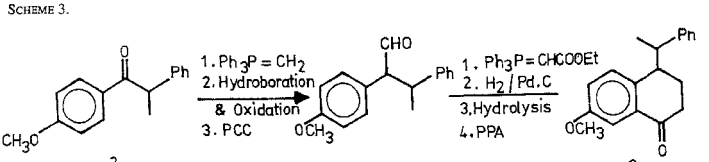

SCHEME 4.

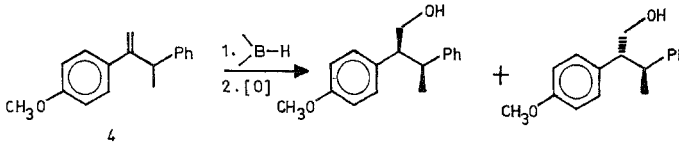

4

SCHEME 5.

References

1. CARAMELLA, P., FRATTINI, P. AND GRUENANGER, P. — Perispecificity in the 1,3-dipolar cycloadditions of benzonitrile oxide with fulvenes, *Tetrahedron Lett.*, 1971, 3817–3820.
2. JACQUES, J., COLLET, A. AND WILEN, S. H. — *Enantiomers, racemates and resolutions*, Ch. 6, 1981, Wiley.
3. CHANDRASEKHAR, S., RAVINDRANATH, M., NEELA, B. S., RAMAKUMAR, S. AND VISWAMITRA, M A. — Cycloaddition of C,N-diphenylnitrone with 6,6-diphenylfulvene, concerted or stepwise? X-ray crystal structure of the product, *J. Chem. Res. (S)*, 1989, 252–253; *J. Chem. Res. (M)*, 1989, 1846–1871.
4. CHANDRASEKHAR, S. AND RAVINDRANATH, M., — Preferential spontaneous resolution of *p*-anisyl α-methylbenzyl ketone, *Tetrahedron Lett.*, 1989, 6207–6208.

Thesis Abstract (Ph.D.)

Luminescence of some d- and f-block elements in alkaline earth–rare earth aluminates, borates and aluminoborates by R. Jagannathan

Research supervisors: T. R. N. Kutty and R. P. Rao (Organization)
Department: Materials Research Centre

1. Introduction

High luminous intensity coupled with good colour rendition is possible with trichromatic deluxe fluorescent lamps which are compatible with human visual system in the spectral region of maximum sensitivity[1]. This is because of the rare-earth luminescent centres in these phosphors wherein the emission is possible from either f-f or d-f transitions. The factors that limit the replacement of less efficient halophosphate phosphor by the trichromatic analogues are: (i) the expensive rare-earth content, and (ii) strict firing conditions under reducing atmosphere at very high temperatures, particularly for the preparation of the blue component. The present investigations address these problems. Hence the choice of the host matrices for these d- and f-block elements was focussed on aluminates, borates and aluminoborates of lanthanides as well as alkaline earths.

2. Preparation and characterization

Preparation of the various borates and aluminoborates is normally accomplished by solid-state reactions at very high temperature[2,3]. In the present case, aluminates were prepared by the hydrothermal method[1]. This method is quite suitable for the preparation of the phosphors with controlled particle size distribution in the range 5–15 μm. All the phosphors prepared were phase-pure, as characterized by X-ray powder diffraction techniques. The luminescence spectra for the various phosphors synthesized were recorded at both room tem-

perature and LNT by using fluorescence spectrophotometer equipped with xenon light source. The other methods used for characterization were wet chemical analysis by AAS, IR spectroscopy for identifying different vibronic species present, and also the EPR spectra for the various luminescent centres (paramagnetic type), so as to have some insight into their local symmetry and the interaction with the immediate environs.

3. Results and discussion

In orthoborates($LnBO_3$, Ln = La, Y & Gd) having aragonite/vaterite-type structure, Eu^{3+} Tb^{3+} yield intense red and green emissions, respectively, corresponding to $^5D_0 \rightarrow {}^7F_2$ transitions. It has also been found that Ce^{3+} is an efficient sensitizer for Tb^{3+}. However, the presence of high-frequency vibrations due to borate group leads to considerable quenching of emission intensities[2]. In the pentaborate system corresponding to $LnMB_5O_{10}$, the luminescence Gd^{3+} in the UV region has been observed. In the polycrystalline pentaborate system we could observe the presence of intense cooperative vibronic transition accompanying electronic transitions. Surprisingly, the same features are absent in the corresponding glass modification. This has been qualitatively explained as due to decreased oscillator strength for the vibronic transition for the glass system, with decreased interionic distances. Furthermore, for the case of Cr^{3+} in $LaCaB_7O_{13}$ (septa-borate system) we observe ^2E-$^4A_2$ line emission and both ^2E-$^4A_2$ (line). $^4T_2$-$^4A_2$ (band) emissions in the polycrystalline and glass systems, respectively. This has been explained in terms of emissions from high and intermediate crystal field sites scheme.

In the case of Mn^{2+} emission in pentaborates, it has been shown that Mn^{2+} occupies a six coordinated noncubic site[3] contrary to reports available in literature. Also the presence of a second kind of Mn^{2+} site, *viz.*, Mn^{2+} - Mn^{2+} dimers has been proved and this has been verified with the help of EPR spectra. But, the Mu^{2+} emission in the pentaborate system has low intensity to merit its applications in lamps. The other demerit with this system is that the emission maximum is located at longer wavelength (630 nm) than the ideal one at 610 nm.

In the pentaborate lattice used as matrix for Mn^{2+} centres, it has been found that Bi^{3+} sensitizes the Mn^{2+} emission efficiently. It is for this reason that the luminescence of Bi^{3+} in this borate system was studied separately. Two types of Bi^{3+} luminescent centres are possible in this system, *viz.*, Bi^{3+} isolated centres and Bi^{3+} clusters. Both these centres sensitize the Mn^{2+} emission efficiently. In addition, it has been found that Bi^{3+} excited state in polycrystalline pentaborate system undergoes dynamic Jahn–Teller distortion while the same is absent in the corresponding glass modification. This has been explained in terms of the absence of symmetry elements and less stiff surroundings of the glass modification.

A new low temperature route, *viz.*, hydrothermal method, is employed for the preparation of the various alkaline earth aluminate/aluminoborate hosts, with Eu^{2+} as the luminescent centre. Through this method, blue-emitting aluminate/aluminoborate-based phosphors with good luminous efficiency comparable to that of the industrial phosphors can be prepared. Also, the particle size distribution of the phosphor powder obtained is very much suitable for lamp applications and is in the range 5–10 μm. Details about a new alkaline earth aluminoborate MAl_3BO_7 are given[4]. In this host lattice, Eu^{2+} yields intense blue emission. It has been found that in $SrAl_3BO_7$: Eu^{2+} system, two types of Eu^{2+} luminescent centres having divergent temperature dependence are present. Also, it has been observed that Eu^{2+}-- Mn^{2+} energy transfer is very efficient in this system. However for some of these aluminoborates (Sr analogue in particular) the Mn^{2+} emission lies at lower wavelength (λ_{em} = 396–400 nm) when compared with the ideal value of 440 nm. Hence, if by proper modification of the host, Eu^{2+} emission can be shifted closer to 440 nm, this will turnout to be potential host for lamp applications.

References

1. KUTTY, T. R. N., JAGANNATHAN, R. AND RAO, R. P. Luminescence of Eu^{2+} in strontium aluminates prepared by hydro thermal methods, *Mater. Res. Bull.*, 1990, **25**, 1355–1362.

2. JAGANNATHAN, R., RAO, R. P. AND KUTTY, T. R. N — Sensitized luminescence of Sm^{3+} $GdBO_3$, *Mater. Chem. Phys.*, 1989, **23**, 329–333.

3. JAGANNATHAN, R., MANOHARAN, S. P. RAO, R. P. AND KUTTY, T. R. N. — Luminescence and energy levels of Mn^{2+} in $LnMB_5O_{10}$, *Jap. J. Appl. Phys.*, 1990, **29**, 1991–1996.

4. JAGANNATHAN, R., RAO, R. P. AND KUTTY, T. R. N — Luminescence of Eu^{2+} in MAl_3BO_7 (M = Sr, Ca & Ba) alumino-borates, *Mater. Res. Bull.*, 1992, **27**, 459–466.

Thesis Abstract (Ph.D.)

Evolutionary design of plan-based pattern recognition systems in complex domains

by Sanjay Rameshchandra Chitnis

Research supervisor: V. V. S. Sarma
Department: Computer Science and Automation

1. Introduction

Cognitive agents live in the world by performing actions to achieve stated goals. The term pattern recognition (PR) refers to a range of cognitive tasks performed by these agents to generate descriptions or models of relevant aspects of the world using available data. These include tasks involving sensory perception such as seeing, hearing, etc., as well as tasks requiring deliberative reasoning such as diagnosis of faults or diseases. These tasks range from simple verification or class labelling to recognition, interpretation or understanding.

The main PR task can be hierarchically broken up into multiple subtasks. Subtasks at the lowest level perform various types of actions: (1) Data gathering actions: These include actions for measurement, such as enabling sensors, setting sensor parameters, etc. (2) Information processing actions: These include signal processing, extraction of features or attributes, identification of primitives, etc. (3) Hypothesis management actions: These include actions for hypothesis formation, refinement, confirmation or rejection. (4) Communication actions: These pertain to communication of processed information or locally generated partial hypotheses to other problem solving units or knowledge structures, such as blackboards as in HEARSAY. (5) Learning actions: These actions upgrade the system online based on its experience. In higher level tasks, actions correspond to the execution of lower level tasks.

Computer scientists have attempted automation of these tasks over the last three decades, with the motivation provided by the need for optical character recognition, speech input to computers, etc. Classically these problems were formulated by using the *classification paradigm* of associating a class label to an object based on certain measured characteristics features, attributes or primitives. The recognition system was implemented in sequential stages of feature or primitive extraction, followed by classification.

Over the years, developments in the field of artificial intelligence (AI) have resulted in a major paradigm shift in performing the recognition task, as well as in the design of PR systems. Initially, the emphasis was on search-based methods while the present focus lies in incorporating domain-specific knowledge at all stages to improve not only the accuracy and efficiency of the system, but also the ability to explain its behaviour and learn from experience.

Designing such systems is an involved *evolutionary* process consisting of multiple stages. This thesis addresses the issues involved in systematic intelligent interactive support of this process within the framework of a *plan-based architecture.*

2. Plan-based architecture

A PR system can be implemented in the form of plans consisting of the optimal (or near-optimal) combination of actions described earlier which specify *what to do* and *when*. From this viewpoint, the task

of *design* becomes that of *planning* for appropriate sequence of actions applicable for different states of problem solving. This leads to a new architecture based on planning to implement knowledge-based PR systems

In this architecture, knowledge is represented in the form of plans. Each plan/subplan consists of *preconditions, a program* of actions, a *rationale* for its usage and information useful for *replanning*. The plans are organized into a *plan library* in one of the two ways: (i) *Deterministic organization*: Here plans are organized hierarchically, *i.e.*, execution of a plan corresponds to an action in the next higher level plan. This fully determines when a plan or a subplan will get executed Such an organization is used when all the problem-solving states are exhaustively enumerable. (ii) *Nondeterministic organization*: Here plans are indexed based on the state of problem solving for which they are applicable. The problem solving occurs in a cycle of assessing the problem-solving state, retrieving the best matching plan, modifying the retrieved plan if necessary, and finally executing the plan. Explanation in this architecture is based on the trace of the plans executed and the contents of the *rationale* slots in those plans.

As compared to the conventional architecture for knowledge-based systems, this architecture is more efficient due to the use of *compiled knowledge* in the form of plans. Each subtask can utilize its own knowledge representation and problem-solving techniques. This architecture, therefore, provides a *uniform framework* for integration of multiple problem solving strategies. It is most *robust* since plans can be generated opportunistically as and when required. It supports the evolutionary process of design naturally through *plan refinement*.

3. Evolutionary design

The inputs to the design process come from three groups of people: the users, the domain experts and the designers. The users specify the requirements of the system, the domain experts provide the necessary domain knowledge, and the designers build the system using this knowledge. Each of these inputs is imperfect and tentative in nature. The requirement specifications given by users are imprecise and/or complete, and evolve over time. The knowledge given by domain experts is generally incomplete, imprecise and uncertain. It is usually in the declarative form and thus does not directly indicate *what to do* and *when*. The designer makes certain decisions during design whose ramifications become clear only after the design is completed and evaluated.

This shows that any particular design is only a tentative solution which needs to be refined again and again until *satisfactory* performance is achieved. We propose a systematic approach to support this evolutionary design cycle as depicted in Fig. 1. We describe the methods and measures appropriate for the tasks involved in this process.

Requirement analysis and specification. At this stage, the user requirements are assessed and a compromise is made on the required functionality and performance level of the system given the available technology and other constraints. These specifications may change during the design cycle. At present, this needs to be done manually.

Knowledge acquisition: In this phase, we first analyze the structure of the given problem to identify the various tasks involved. For each of these tasks, we acquire, organize and represent the necessary knowledge from

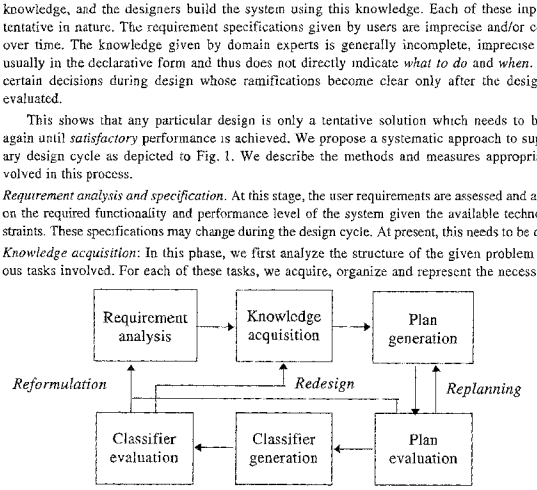

FIG. 1. Evolutionary desing process.

human experts and other knowledge sources. Although the human experts are good at the PR task, they often cannot articulate how they recognize. They can verbalize only the *declarative model* of the domain. It consists of. (1) *category structure*: multiple, possibly incomplete and imprecise definitions of categorical concepts and their interrelationships (including likelihood information); (2) *available actions*; (3) *dependencies* between the actions and the parameters of the world; (4) *feasibilty* of actions under the given circumstances (constraints); and finally, (5) *desirability* of the consequences.

We represent all facets of this knowledge in the form of hierarchical influence diagrams. Influence diagrams are directed acyclic graphs with nodes representing various domain concepts and actions, and arcs representing various kinds of interrelationships between them. Corresponding to each task we have one influence diagram whose action nodes correspond to subtasks. This graphical representation aids the process of knowledge elicitation by making human experts *see* explicitly what they are trying to convey. Influence diagrams are superior to other knowledge structures such as rules, frames, decision trees, etc., for representing PR domain knowledge, because they can represent all facets of the available knowledge in one compact structure.

This structure was originally used in decision analysis. We have adapted and extended it to pattern recognition problems with hierarchical domain structure, Dempster–Shafer theory (DST)-based likelihood information and possibly hostile environment. We provide an algorithm for estimating likelihood information in the form of DST belief functions from labelled samples.

Plan generation: At this stage, we *operationalize* the declarative domain knowledge given by human experts, *i.e.*, we generate procedural knowledge in the form of plans from the declarative knowledge in the form of a domain model. Plans can be generated afresh or can be refined from an existing plan using feedback generated from the *plan evaluation* stage.

We describe several new techniques and heuristic measures for plan generation and plan refinement. Deterministic plans are generated using a new algorithm based on heuristic search. It uses a new γ *cutoff* for pruning in addition to α and β, which are used in game trees. We define a new heuristic measure called *merit* for each evidence gathering action, to improve the efficiency of the plan generation process. This measure is defined as the ratio of another heuristic measure–*discrimination ability* and the cost of the action. Discrimination ability is defined using the belief function corresponding to the evidence generated by an action. It takes into account the precision and accuracy of the evidence. Search efficiency is improved by using various *node ordering strategies*. *Meta-level decisions* are introduced in the plan which help in postponing the making of certain assumptions during the plan generation. For example, decisions about actual time and resource constraints, capacity to absorb loss, etc., are postponed till plan execution time.

To generate a nondeterministic plan, we first analyze the appropriate influence diagrams to find possible significant states of problem solving. For each such state, we order the functions for execution based on their *merit* values. Finally, we generate an indexed structure to represent this kind of plan.

Plan evaluation: We evaluate the generated plans to get directions for further improvements.

We propose some new measures for this purpose. Nondeterministic plans are evaluated based on a new heuristic called the *index of focusing*. For deterministic plans, we perform *value of information* analysis to find out which tasks or actions need further refinement. Suggestions for changes in system specifications to improve the performance while maintaining the functionality of the system are generated using *value of control* analysis.

Classifier generation: In this stage, we compile the plan expressed using *plan language* into an executable code for the classifier

Classifier evaluation: Performance of the designed classifier is assessed with respect to various criteria such as error rate, precision, recall, total cost, etc. If the generated classifier does not satisfy the user requirements, the cycle is repeated with either the addition of extra knowledge and *redesign* of the system or *reformulation* of the user specifications.

We use a simple two-class two-feature problem to explain and clarify the proposed techniques and measures.

4. Implementation results

A *design environment* which supports this evolutionary process has been implemented on a SUN workstation. It consists of around 15000 lines of COMMON LISP (including COMMON LISP OBJECT SYSTEM) and LEX code We evaluate this methodology using the following four PR problems of progressively increasing complexity.

4.1. *Classification of IRIS flowers*

This is a common example used in PR literature for testing discriminant analysis and clustering algorithms. A standard data set of measurements on IRIS flowers which was collected by Anderson and first used by Fisher is generally used for this purpose. There are 50 samples each for the three classes: *Iris setosa, Iris versicolor and Iris virginica*. For each sample, four measurements were taken: sepal length, sepal width, petal length and petal width. In addition to these measurements, we use two more derived features—petal shape and sepal shape. We use this classical example to demonstrate the systematic plan generation process. DST belief functions are estimated from the training samples. The classifier gives 5.33% error rate when designed with 50% of the samples for training and the rest for testing.

4.2. *Identification of Indian names*

Given an alphabetic string of a person's name, we want to decide whether the name is of Indian origin or not. This is a pattern verification problem with one class denoting the concept of names of *Indian origin* and the other class representing the amorphous union of all other names. We use three different techniques for this purpose: (1) *Lexicon based*; We have prepared a lexicon of common Indian names and nonIndian names. If a name is found, we can make a decision with 100% certainty. Otherwise there is complete ignorance. (2) *Trigram based*: We estimate the probability of the name being Indian from the probability of every three consecutive phonemes occurring in the name. The required probabilities are learnt from the training samples. (3) *Pattern based*: We make decision based on the common patterns occurring in the name. These patterns were given by human experts.

We use this problem to evaluate the efficacy of the new pruning technique based on α-β-γ cutoffs. We also demonstrate evolutionary improvement in the design using the plan refinement technique based on value-of-information analysis. The final classifier classifies 92.27% samples correctly from the test set of 5857 samples.

4.3. *Voice-operated telephone dialler*

A voice-operated telephone dialler enables users to access various services offered by a telephone exchange through a speech by interface. It is a *limited vocabulary isolated word recognition system* usable in moderately noisy environments for a limited number of cooperative speakers. The words in the lexicon include the digits zero to nine, names of the cities for subscriber trunk dialling and commands to the exchange for the services and to the dialler itself such as connect, redial, cancel, etc. The input sentence is expected to follow the syntax and semantics of the protocol designed for accessing the services. The input of the system is taken through the mouthpiece of the telephone and the output, which is the sequence of numbers to be dialled, is displayed back for verification and possible correction.

In this example, we demonstrate the use of hierarchical influence diagrams for knowledge representation, nondeterministic organization of the plan library and redesign explorations based on value-of-information and value-of-control analyses. The final system design achieves a recognition accuracy of 93.33% using simple features.

4.4. *Multisensor integration and situation assessment*

Multisensor integration and situation assessment (MSI/SA) involves maintaining an up-to-date perception of the world for a decision maker by continuous and synergistic combination of data/information gathered from

diverse sources such as sensors, intelligence reports, databases, etc., together with prior domain knowledge in a hostile environment such as a battlefield. The physical architecture of such systems consists of a network of sites linked by communication channels. Each site contains multiple sensors and a local fusion agent. Each site receives a global situation assessment from a central site and sends its local assessment which is based on reports from the local sources. A site may also communicate with its neighbouring sites.

This domain is special due to the presence of an adversary, the need for communication in a distributed environment, and the possibilities of zero sum/nonzero sum values and complete/incomplete information. Using a set of examples such as active sensor management, prisoner's dilemma, etc., we demonstrate the advantage of enhanced influence diagram representation for domain modelling and plan generation for generating decision strategies.

5. Conclusions

The evolutionary design paradigm is found to be effective for pattern recognition systems in complex domains. The plan-based architecture is found inherently suitable for supporting evolutionary design in addition to its other advantages such as its generality and flexibility with respect to integrating multiple problem-solving strategies and improved efficiency because of the procedural knowledge representation. We believe that this methodology has considerable potential for application in a wider class of problems such as intelligent decision support systems and C^3I systems.

References

1. OLIVER, R M. AND SMITH, J. Q. (eds) *Influence diagrams, belief nets and decision analysis* 1990, Wiley.

2. DASGUPTA, S. *Design theory and computer science: Processes and methodology of computer systems design*, 1991, Cambridge University Press.